

An ATG16L1-dependent pathway promotes plasma membrane repair and limits *Listeria monocytogenes* cell-to-cell spread

Joel M. J. Tan^{1,2,18}, Nora Mellouk^{1,18}, Suzanne E. Osborne¹, Dustin A. Ammendolia^{1,3}, Diana N. Dyer^{1,3}, Ren Li¹, Diede Brunen⁴, Jorik M. van Rijn⁴, Ju Huang¹, Mark A. Czuczman^{1,3}, Marija A. Cemna^{1,3}, Amy M. Won⁵, Christopher M. Yip⁵, Ramnik J. Xavier⁶, Donna A. MacDuff⁷, Fulvio Reggiori^{4,8}, Jayanta Debnath⁹, Tamotsu Yoshimori¹⁰, Peter K. Kim^{1,11}, Gregory D. Fairn^{11,12}, Etienne Coyaud¹³, Brian Raught^{13,14}, Aleixo M. Muise^{1,11,15,16}, Darren E. Higgins¹⁷ and John H. Brumell^{1,2,3,16*}

Plasma membrane integrity is essential for the viability of eukaryotic cells. In response to bacterial pore-forming toxins, disrupted regions of the membrane are rapidly repaired. However, the pathways that mediate plasma membrane repair are unclear. Here we show that autophagy-related (ATG) protein ATG16L1 and its binding partners ATG5 and ATG12 are required for plasma membrane repair through a pathway independent of macroautophagy. ATG16L1 is required for lysosome fusion with the plasma membrane and blebbing responses that promote membrane repair. ATG16L1 deficiency causes accumulation of cholesterol in lysosomes that contributes to defective membrane repair. Cell-to-cell spread by *Listeria monocytogenes* requires membrane damage by the bacterial toxin listeriolysin O, which is restricted by ATG16L1-dependent membrane repair. Cells harbouring the ATG16L1 T300A allele associated with inflammatory bowel disease were also found to accumulate cholesterol and be defective in repair, linking a common inflammatory disease to plasma membrane integrity. Thus, plasma membrane repair could be an important therapeutic target for the treatment of bacterial infections and inflammatory disorders.

Pore-forming toxins (PFTs) are crucial virulence factors produced by many bacterial pathogens¹. PFTs permeabilize host cell membranes, typically targeting the plasma membrane but also intracellular organelles, thereby promoting the influx or efflux of ions, small molecules and proteins. Although PFTs can cause cell death, sublytic doses induce pleiotropic cellular responses, including plasma membrane repair, inflammasome activation and metabolic changes^{2,3}. Furthermore, bacterial pathogens can utilize PFTs to promote distinct stages of their pathogenic lifestyle⁴. For example, listeriolysin O (LLO, encoded by the *hly* gene) is a PFT expressed by *Listeria monocytogenes* (*Lm*) that promotes bacterial growth in vacuoles⁵, blocks phagosome acidification to allow bacterial escape into the cytosol⁶, induces organelle modifications⁷, and promotes cell-to-cell spread by damaging the plasma membrane⁸. The membrane-damaging activity of LLO is actively countered

by host cell membrane repair pathways, maintaining cell viability amidst PFT attack^{8,9}.

Rapid plasma membrane repair in response to PFTs is crucial for cell survival but the molecular mechanisms employed by cells to maintain membrane integrity remain poorly understood. Calcium influx induced by PFTs is a key messenger strictly required for plasma membrane repair¹⁰. Multiple mechanisms to promote Ca²⁺-dependent repair include: cell surface blebbing, lysosome exocytosis, endocytosis and microvesicle shedding¹¹. Plasma membrane blebbing, a process by which actomyosin contractions drive the detachment of the plasma membrane from the actin cortex, is thought to create a confined space enriched in Ca²⁺, thereby favouring membrane repair^{12,13}. Additionally, lysosomal exocytosis is known to promote membrane repair by increasing the cell surface and relieving plasma membrane tension¹⁴.

¹Cell Biology Program, Hospital for Sick Children, Toronto, Ontario, Canada. ²Institute of Medical Science, University of Toronto, Toronto, Ontario, Canada. ³Department of Molecular Genetics, University of Toronto, Toronto, Ontario, Canada. ⁴Department of Cell Biology and Institute of Biomembranes, University Medical Center Utrecht, Utrecht, the Netherlands. ⁵Institute of Biomaterials and Biomedical Engineering, University of Toronto, Toronto, Ontario, Canada. ⁶Gastrointestinal Unit and Center for the Study of Inflammatory Bowel Disease, Massachusetts General Hospital, Harvard Medical School, Boston, MA, USA. ⁷Department of Microbiology and Immunology, University of Illinois at Chicago College of Medicine, Chicago, IL, USA. ⁸Department of Cell Biology, University of Groningen, University Medical Centre Groningen, Groningen, The Netherlands. ⁹Department of Pathology and Helen Diller Family Comprehensive Cancer Center, University of California, San Francisco, CA, USA. ¹⁰Department of Cellular Regulation and Host Defense, Research Institute for Microbial Diseases, Osaka University, Osaka, Japan. ¹¹Department of Biochemistry, University of Toronto, Toronto, Ontario, Canada. ¹²Keenan Research Centre for Biomedical Science, St. Michael's Hospital, Toronto, Ontario, Canada. ¹³Princess Margaret Cancer Centre, University Health Network, Toronto, Ontario, Canada. ¹⁴Department of Medical Biophysics, University of Toronto, Toronto, Ontario, Canada. ¹⁵Division of Gastroenterology, Hepatology, and Nutrition, Department of Paediatrics, Hospital for Sick Children, Toronto, Ontario, Canada. ¹⁶SickKids IBD Centre, Hospital for Sick Children, Toronto, Ontario, Canada. ¹⁷Department of Microbiology and Immunobiology, Harvard Medical School, Boston, MA, USA. ¹⁸These authors contributed equally: Joel M. J. Tan, Nora Mellouk. *e-mail: john.brumell@sickkids.ca

Macroautophagy (hereafter autophagy) is a cellular pathway that delivers proteins, organelles and microbial pathogens to the lysosome for degradation¹⁵. More than 30 autophagy-related (ATG) proteins regulate this pathway and act in a highly conserved manner in eukaryotes. In mammals, many ATG proteins also serve roles in other distinct cellular pathways¹⁶. Dysregulated autophagy has been linked to many human diseases, such as inflammatory bowel disease (IBD), although the mechanisms by which genetic variants of autophagy genes contribute to human disease are unclear¹⁵. Autophagy has recently been linked to cell autonomous resistance to PFTs. Loss of expression of individual ATG proteins was found to increase toxin-mediated damage to the plasma membrane^{17–19}. However, it is not known whether autophagy or other ATG-dependent pathways mediate toxin resistance.

Here we examined the role of ATG proteins in cell autonomous resistance to bacterial PFTs. We show that ATG16L1 and its binding partners ATG5 and ATG12 promote plasma membrane repair by a pathway independent of canonical autophagy. Our study reveals an important role for ATG16L1 in lysosomal exocytosis and cytoprotective blebbing responses, both contributing to plasma membrane repair upon PFT damage. ATG16L1 deficiency was found to cause accumulation of cholesterol in lysosomes that contributes to defective membrane repair. ATG16L1 was also found to restrict cell-to-cell spread of *Lm* by limiting LLO-mediated membrane damage. Our study has important implications for understanding the role of ATG16L1 in innate immunity and its links to human diseases such as IBD.

Results

ATG16L1 contributes to toxin resistance by a pathway distinct from canonical autophagy. We examined the role of ATG in cellular resistance to the Pneumolysin (Ply) toxin from *Streptococcus pneumoniae*, a member of the cholesterol-dependent cytolysin (CDC) family of bacterial toxins^{1,2}. Mouse embryonic fibroblasts (MEFs) derived from *Atg* knockout (KO) mice and their respective wild-type (WT) controls were examined. Cells were treated with sublytic doses of Ply and propidium iodide, a cell-impermeant nucleic acid dye, was used to measure toxin-induced membrane damage (Fig. 1a). Because plasma membrane repair is a Ca²⁺-dependent process², the absence of extracellular Ca²⁺ allows us to visualize the full extent of membrane damage induced by toxin treatment.

In the presence of extracellular Ca²⁺, MEFs lacking ATG5, ATG12 and ATG16L1 displayed higher levels of propidium iodide uptake compared to control MEFs (Fig. 1b,c). In contrast, loss of the autophagy components RUBICON, ATG3, ATG9 and ATG14 did not affect toxin resistance (Fig. 1b,c and Supplementary Fig. 1a). In the absence of extracellular Ca²⁺, extensive propidium iodide uptake was observed in all MEFs, suggesting that toxin damage was equivalent in the absence of plasma membrane repair pathways, regardless of the different ATG expression status. Similarly in HeLa cells, ATG16L1 KO increased propidium iodide uptake but not ATG3 KO (Supplementary Fig. 8a,b). Damage to the plasma membrane leads to a loss of membrane asymmetry and the exposure of exofacial phosphatidylserine²⁰. MEFs lacking ATG5, ATG12 and ATG16L1 displayed higher levels of exofacial phosphatidylserine, consistent with our findings in the propidium iodide uptake assay (Supplementary Fig. 2a,b). MEFs lacking ATG16L1 were also susceptible to damage by digitonin, a steroidal saponin (Supplementary Fig. 1b,c). Using live cell imaging of WT MEFs, we did not observe recruitment of ATG16L1 or the autophagy marker microtubule associated light chain 3-B (LC3B) to the plasma membrane in response to Ply treatment (Supplementary Fig. 1e,f). As ATG16L1 can exist in a multimeric complex with conjugates of ATG5 covalently linked to ATG12¹⁵, our studies indicate these members contribute to toxin/digitonin resistance by a pathway distinct from canonical autophagy.

The IBD-associated T300A variant of ATG16L1 impairs toxin resistance. The rs2241880 genetic variant of *ATG16L1* (leading to a T300A conversion) has been linked to several human diseases including IBD²¹, susceptibility to bacterial infection^{22,23}, necrotizing enterocolitis²⁴ and gastric cancer in humans²⁵. To examine the impact of the ATG16L1 T300A variant in membrane repair, we took advantage of MEFs expressing a genome-encoded mutant of ATG16L1 lacking its coiled coil domain (ATG16L1 Δ CCD, Fig. 1d)²⁶. This mutant lacks the ATG5-12 binding site and is non-functional. In these cells, we observed an increase in Ply-mediated membrane damage compared to control MEFs, indicating that ATG5-12 binding is required for ATG16L1 to promote membrane repair (Fig. 1e). Stable expression of the human full-length ATG16L1 was sufficient to reduce Ply-mediated membrane damage in ATG16L1 Δ CCD MEFs (Fig. 1e and Supplementary Fig. 1d). In contrast, stable expression of the T300A variant did not reduce Ply-mediated membrane damage. Similarly, deletion of the C-terminal WD domain of ATG16L1 also impaired the ability of ATG16L1 to suppress toxin damage. Thus, expression of the IBD risk allele T300A impairs toxin resistance.

ATG16L1 contributes to toxin resistance by promoting plasma membrane repair. Toxin resistance reflects a balance of both toxin-mediated damage events and cell-mediated repair mechanisms. We considered the possibility that ATG16L1 impacts Ply binding to host cells. To test this, a Ply titration assay was conducted in Ca²⁺-free medium to prevent membrane repair. Cells were treated with decreasing concentrations of Ply from sublytic to undetectable damage levels (Fig. 2a). ATG16L1 KO MEFs and WT controls displayed equivalent membrane damage at all toxin concentrations (Fig. 2b). We also examined direct binding of toxin to cells using an enhanced green fluorescent protein fusion to Ply (EGFP-Ply)²⁷. Binding of EGFP-Ply to MEFs was not affected by loss of ATG16L1 as determined by fluorescence microscopy (Fig. 2c) and flow cytometry (Fig. 2d). We also considered the possibility that ATG16L1 impacts exofacial plasma membrane cholesterol, which may affect binding of CDCs. Using the HIS6X-GFP-D4 probe to visualize plasma membrane cholesterol²⁸, ATG16L1 WT and KO MEFs displayed similar fluorescence intensity assessed by flow cytometry (Fig. 2e). Thus, ATG16L1 deficiency does not affect Ply binding or damage.

A cholesterol-independent membrane wounding assay was also performed by scraping the cells and allowing them to repair. ATG16L1 KO MEFs were deficient in membrane repair indicated by an increase in PI⁺ cells (Fig. 2f), recapitulating the KO repair defect seen by toxin treatment. Our findings suggest a general role for ATG16L1 in plasma membrane repair.

To monitor the recovery kinetics of plasma membrane repair, we performed a toxin pulse-chase assay (Fig. 2g). Cells were treated with Ply followed by the addition of propidium iodide at different times post-Ply treatment. Control HeLa and MEF cells displayed rapid resealing of the plasma membrane within minutes, as assessed by low PI⁺ cells at all time points (Fig. 2h and Supplementary Fig. 8c). In contrast, ATG16L1 KO MEFs and ATG12 siRNA KD HeLa cells displayed a strong impairment in plasma membrane repair that persisted for at least 5 min following toxin treatment. Our findings suggest that ATG16L1 plays an important role in promoting rapid plasma membrane repair.

ATG16L1 promotes lysosomal exocytosis and plasma membrane bleb formation. We tested whether ATG16L1 impacts any of the known plasma membrane repair pathways²⁹. Annexins are recruited to sites of membrane damage in response to calcium influx², while endosomal sorting complexes required for transport (ESCRT) recruitment to the plasma membrane also promotes membrane repair of small wounds³⁰. Using live cell imaging, we visualized the recruitment of GFP fusions to ESCRT component CHMP4B,

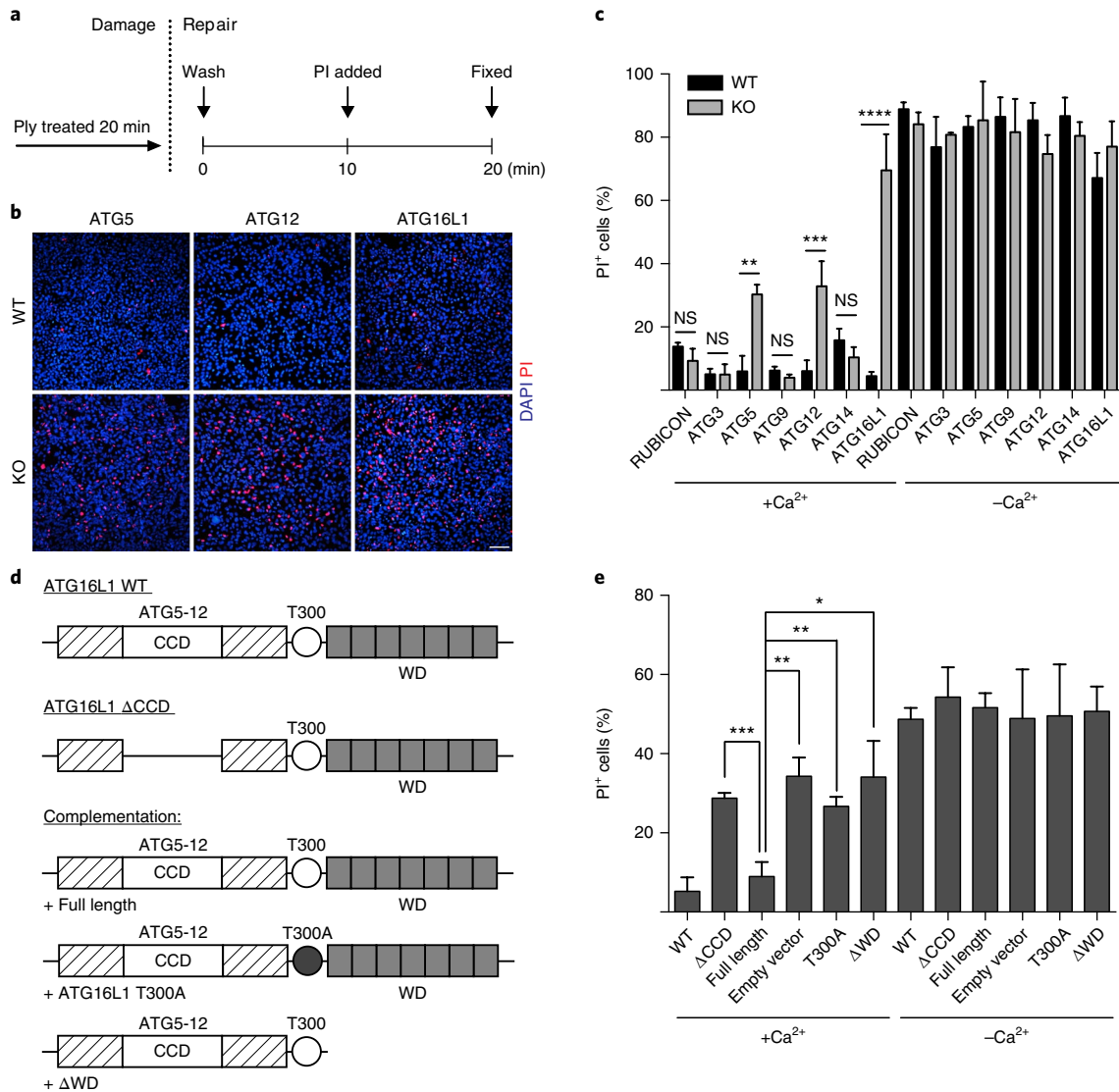


Fig. 1 | ATG16L1 contributes to toxin resistance by a pathway distinct from canonical autophagy. **a**, Experimental design for Ply toxin treatment. PI, propidium iodide. **b**, MEFs from the indicated *Atg* KO and their respective controls (WT) were treated with Ply (200 ng ml⁻¹) and membrane integrity was assessed with propidium iodide labelling. Cells were then fixed and DNA was labelled with DAPI. Scale bar, 70 μm. Images are representative of three independent experiments. **c**, MEFs were treated as in **a** and PI⁺ cells were enumerated ($N = 30,000$ – $40,000$ cells). **d**, Schematic of WT ATG16L1 and mutants studied. **e**, Control or ATG16L1-deficient (Δ CCD) MEFs ectopically expressing the indicated human ATG16L1 construct were treated as in **a** and PI⁺ cells were enumerated ($N = 30,000$ – $40,000$ cells). **c, e**, Data shown are means \pm standard deviation (s.d.) for three independent experiments. P value was calculated using two-way analysis of variance (ANOVA) (**c**) and one-way ANOVA (**e**). * $P < 0.05$, ** $P < 0.01$, *** $P < 0.001$, **** $P < 0.0001$, not significant (NS) > 0.9999 .

Annexins-1, -2 and -6 to the plasma membrane in response to Ply damage. ATG16L1 deficiency did not affect Annexins or ESCRT translocation from the cytosol to the plasma membrane on Ply treatment (Supplementary Fig. 3). Our findings suggest that ATG16L1's role in plasma membrane repair is unrelated to annexins and ESCRT recruitment observed in this process.

Ca²⁺-triggered exocytosis of lysosomes also promotes plasma membrane repair of both small wounds (by PFTs) and large wounds (by mechanical damage)^{14,31}. We examined lysosomal exocytosis in Ply toxin treated cells by measuring delivery of the lysosome transmembrane protein LAMP1 to the plasma membrane, as previously described³². Cells were stained on ice with a monoclonal antibody recognizing an exofacial epitope present on LAMP1 after membrane insertion. In control MEFs, we observed exofacial LAMP1 at sites of membrane damage marked by exofacial phosphatidylserine

(Fig. 3a). ATG16L1 KO MEFs displayed a decrease in levels of exofacial LAMP1 at sites of membrane damage induced by Ply (Fig. 3a, b). Total intracellular LAMP1 levels were not affected by ATG16L1 deficiency (Supplementary Fig. 4a–c). Therefore, ATG16L1 is required for the lysosomal exocytosis during plasma membrane repair upon toxin damage.

The formation of cell surface blebs has been shown to promote resistance to bacterial toxins¹². Using the cytosolic marker CellTracker Green, we performed live cell imaging to examine blebbing responses during Ply treatment. In control MEFs, we observed rapid formation of large blebs at the cell surface (Fig. 3c). ATG16L1 KO MEFs displayed more blebs after toxin treatment (Fig. 3c, d). By tracking bleb formation live, we determined that bleb size was significantly smaller in ATG16L1 KO cells (Fig. 3c, e). Blebs are dynamic structures that can retract to the cell body during recovery from

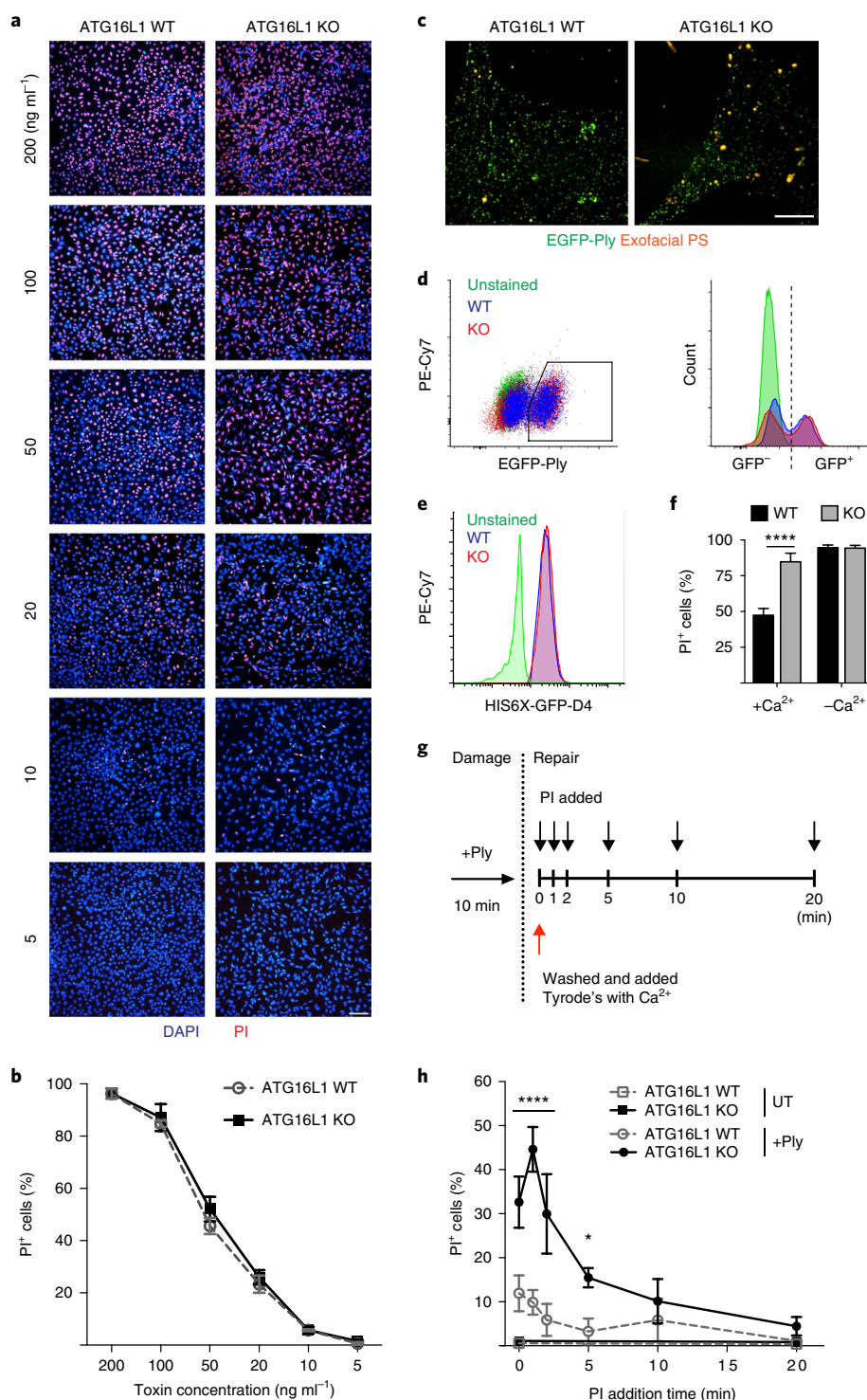


Fig. 2 | ATG16L1 contributes to toxin resistance by promoting plasma membrane repair. **a**, MEFs were treated with sublytic concentrations (5–200 ng ml⁻¹) of Ply in Tyrode's buffer without Ca²⁺ to measure membrane damage. Images are representative of three independent experiments. Scale bar, 70 μ m. **b**, ATG16L1 WT and KO MEFs were treated as in **a** and PI⁺ cells were enumerated ($N=30,000$ –40,000 cells). **c**, Confocal images from three independent experiments of ATG16L1 WT and KO MEFs treated with EGFP-Ply to measure toxin binding. Scale bar, 11 μ m. **d**, Flow cytometric data from three independent experiments of ATG16L1 WT and KO MEFs treated with EGFP-Ply to measure toxin binding. PS, phosphatidylserine. **e**, Flow cytometric data from three independent experiments of ATG16L1 WT and KO MEFs treated with HIS6X-GFP-D4 to measure exofacial plasma membrane cholesterol. **f**, Plasma membrane of MEFs was mechanically damaged by scraping, and membrane repair assessed by propidium iodide entry using flow cytometry ($N=50,000$ cells). **g**, Schematic of the pulse-chase experiment. ATG16L1 WT and KO MEFs were treated with Ply for 10 min to allow membrane damage to occur (pulse). Cells were then washed in Tyrode's buffer with Ca²⁺ to remove Ply (chase) and to allow membrane repair to occur. Cells were stained with propidium iodide at the indicated time points (denoted by arrows). **h**, Flow cytometry used to quantify the percentage of cells that stained positive for propidium iodide at each time point ($N=50,000$ –100,000 cells). UT, untreated. All data shown as mean \pm s.d. for three independent experiments. P value was calculated using two-way ANOVA. * $P < 0.05$, **** $P < 0.0001$.

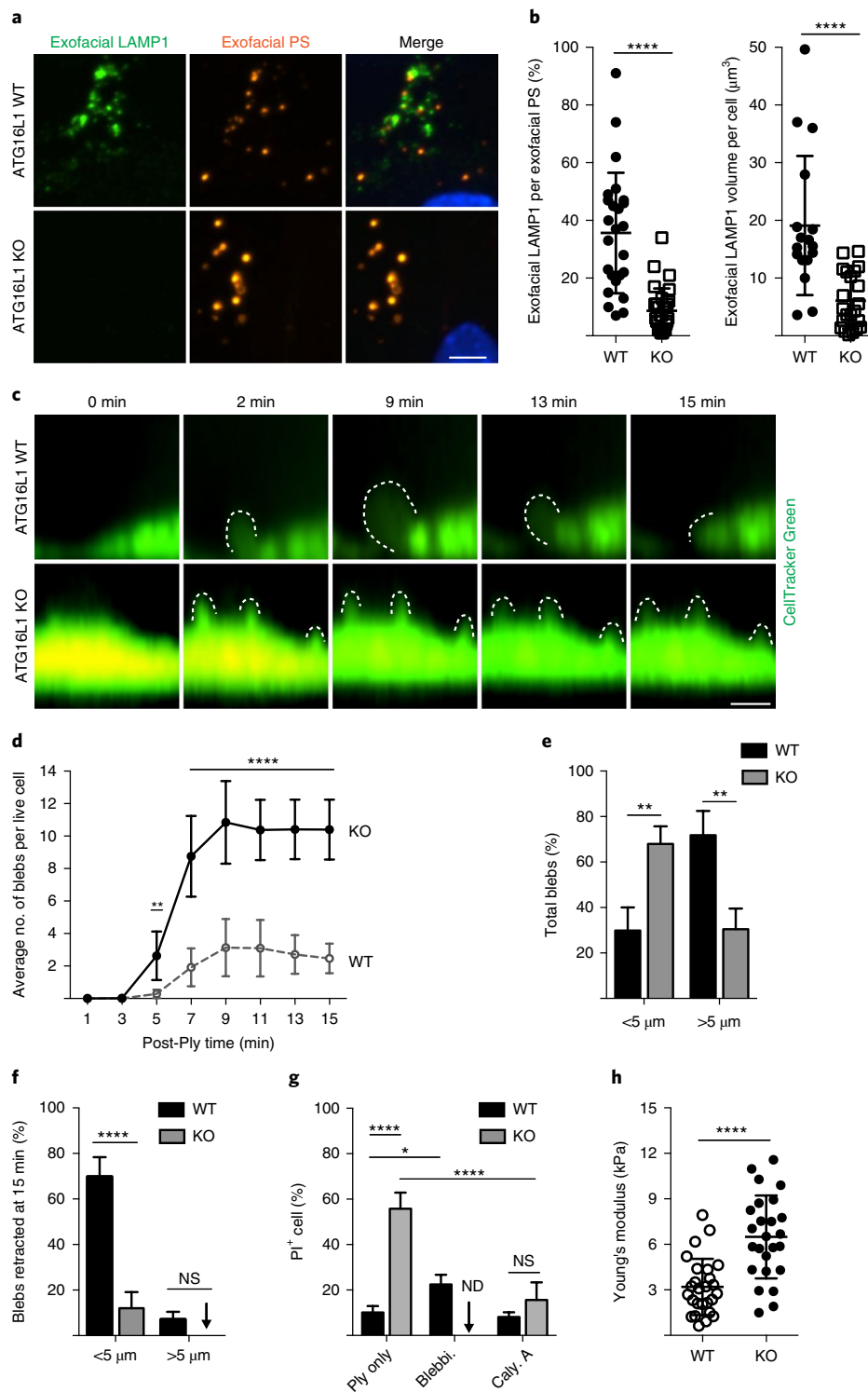


Fig. 3 | ATG16L1 promotes lysosome exocytosis and plasma membrane bleb formation. **a**, Representative images of ATG16L1 WT and KO MEFs treated with Ply and stained for exofacial lysosome marker LAMP1 and exofacial phosphatidylserine. Images are representative of three independent experiments. **b**, Exofacial LAMP1 volume per cell was quantified and normalized to the volume of exofacial phosphatidylserine (PS) signal ($N=400$ cells). P value was calculated using a two-tailed Mann-Whitney test. **c**, ATG16L1 WT and KO MEFs were labelled with CellTracker Green and treated with Ply toxin. Representative live cell imaging of bleb formation and retraction from three independent experiments. **d**, Bleb formation per cell was tracked over the time course of the live cell image ($N=225$ cells). P value was calculated using one-way ANOVA. **e**, Average bleb size was measured as large blebs (>5 μm) or small blebs (<5 μm). **f**, Total bleb retraction was enumerated and stratified according to bleb size. **g**, ATG16L1 WT and KO MEFs were subjected to a propidium iodide assay in the presence of blebbistatin (100 μM) or calyculin A (20 μM). Number of PI⁺ cells were enumerated ($N=30,000$ –40,000 cells). P value was calculated using two-way ANOVA. ND, not determined; NS, not significant. **h**, Atomic force microscopy was performed on ATG16L1 WT and KO MEFs to measure basal levels of membrane tension ($N \geq 25$ cells). All data shown as mean \pm s.d. for three independent experiments. P value was calculated using two-tailed Mann-Whitney test. * $P < 0.05$, ** $P < 0.01$, **** $P < 0.0001$, NS > 0.9999. Scale bars, 11 μm .

plasma membrane damage¹². We observed that in ATG16L1 KO MEFs the majority of blebs did not retract after 15 min (Fig. 3c,f).

Bleb formation is mediated by actin–myosin contractility, which can be manipulated using drugs to induce or prevent bleb formation^{12,13}. Treatment of control MEFs with the myosin II inhibitor blebbistatin caused an increase in membrane damage (reflected by propidium iodide uptake), consistent with previous findings¹² (Fig. 3g and Supplementary Fig. 4d,e). ATG16L1 KO MEFs did not survive Ply treatment in the presence of blebbistatin, revealing an extreme sensitivity to this drug and toxin combination. Treatment of ATG16L1 KO MEFs with calyculin A, a phosphatase inhibitor that promotes actin–myosin contractility and bleb formation^{12,13}, caused a significant decrease in membrane damage induced by Ply (Fig. 3g and Supplementary Fig. 4d,e). Because bleb expansion is regulated by cortical tension³³, we used atomic force microscopy to measure basal membrane rigidity. We observed higher membrane tension in ATG16L1 KO MEFs (Fig. 3h), which implicates a role of ATG16L1 in the biophysical properties of the plasma membrane.

ATG16L1 deficiency causes intracellular cholesterol accumulation. Cholesterol is known to regulate stiffness of the plasma membrane³⁴ and exocytosis of lysosomes³⁵. ATG5 was previously shown to mediate cholesterol efflux from macrophage foam cells by a mechanism that remains poorly characterized³⁶. Based on these findings, we hypothesized that ATG16L1 may promote membrane repair by affecting cellular cholesterol.

We measured cellular cholesterol using a biochemical (Amplex red) assay. MEFs lacking ATG5, ATG12 or ATG16L1 displayed higher levels of cholesterol compared to control MEFs (Fig. 4d), while loss of ATG3 did not affect cholesterol levels. Accordingly, we observed increased binding of filipin to ATG16L1 KO cells compared to control cells (Fig. 4a).

As an alternative method to visualize intracellular cholesterol, we used the cholesterol biosensor mCherry-D4H. When mCherry-D4H is expressed in the cytosol it binds cholesterol on the cytosolic leaflet of the plasma membrane and intracellular organelles. Using this probe, we observed that HeLa and MEF cells lacking ATG5, ATG12 or ATG16L1 displayed higher levels of cholesterol compared to control cells (Fig. 4b,c and Supplementary Fig. 8d,e). In contrast, ATG3 KO did not affect mCherry-D4H fluorescence compared to control. Cholesterol accumulation was also observed in ATG16L1 Δ CCD MEFs (Fig. 4e). Stable expression of the human full-length ATG16L1, but not the T300A variant or Δ WD deletion mutant, was sufficient to reduce cellular cholesterol. Our studies indicate that ATG16L1 and its binding partners ATG5 and ATG12 play a role in regulating cellular cholesterol independently from canonical autophagy pathways.

To further examine the impact of ATG16L1 on cellular cholesterol, we obtained tissues from the small intestine of ATG16L1^{fllox/fllox} Villin-Cre mice. Filipin staining revealed an increase in cellular cholesterol indicated by a higher fluorescence intensity of ATG16L1 Cre⁺ small intestine relative to control (Cre⁻) mice (Fig. 4f,g). Our studies indicate an important role for ATG16L1 in regulating cellular cholesterol in intestinal epithelial cells in vivo.

Cholesterol accumulation in ATG16L1-deficient cells impairs membrane repair and lysosomal exocytosis. Cholesterol accumulation in late endocytic compartments can be induced using U18666A, a drug that blocks the lysosome cholesterol transporter NPC1³⁷. Conversely, T0901317 is an LXR agonist that promotes ABCA1 transporter insertion into the plasma membrane, which reduces intracellular cholesterol by increasing cholesterol efflux³⁸. Consistent with previous findings, U18666A treatment was sufficient to increase intracellular cholesterol (as measured by mCherry-D4H probe intensity) in control MEFs, but not in ATG16L1 KO

cells (Fig. 4h,i). Conversely, T0901317 showed a decrease in intracellular cholesterol in the ATG16L1-deficient MEFs.

We examined plasma membrane repair upon Ply and drug treatments. Increasing cholesterol in late endocytic compartments with U18666A impaired plasma membrane repair in control MEFs (Fig. 5a,b). Thus, this treatment phenocopies the defect in membrane repair observed in ATG16L1 KO cells by elevating cholesterol. Lowering intracellular cholesterol in the ATG16L1 KO cells by treatment with T0901317 was sufficient to restore plasma membrane repair. In the absence of extracellular Ca²⁺, extensive membrane damage was observed in all conditions, indicating toxin damage was equivalent with these drug treatments. Our findings indicate that elevated cholesterol contributes to the inhibition of plasma membrane repair observed in ATG16L1-deficient cells.

We then determined the impact of cholesterol accumulation on lysosomes. We observed a strong association of mCherry-D4H with LAMP1⁺ compartments in ATG16L1-deficient MEFs (Fig. 5c,d). Cholesterol accumulation on LAMP1⁺ compartments was also observed in control MEFs treated with U18666A. Treatment of ATG16L1-deficient MEFs with T0901317 was sufficient to reduce cholesterol on LAMP1⁺ compartments. To determine the impact of cholesterol accumulation on lysosomal exocytosis, we treated cells with ionomycin, a calcium ionophore³⁵. In control MEFs, we observed rapid lysosomal exocytosis, which could be blocked by treatment with U18666A (Fig. 5e,f). In contrast, ATG16L1-deficient MEFs did not display lysosome exocytosis in response to ionomycin. However, treatment of ATG16L1-deficient MEFs with T0901317 partially rescued this phenotype. ATG16L1 WT and KO treated with Ply showed the same trends as ionomycin (Supplementary Fig. 5a,b). Treatment of cells with U18666A or T0901317 alone had no effect on lysosomal exocytosis (Supplementary Fig. 5c). Therefore, our findings indicate that elevated levels of cholesterol present on LAMP1⁺ compartments contribute to defective plasma membrane repair observed in ATG16L1-deficient cells.

ATG16L1 limits cell-to-cell spread of *Lm* by promoting plasma membrane repair. Listeriolysin O belongs to the same CDC family of toxins as Ply, and plays a major role in the virulence of *Lm*¹⁴. These bacteria undergo actin-based motility in the cytosol of host cells and generate cell surface protrusions that can be internalized by neighbouring cells, thereby promoting bacterial dissemination³⁹. LLO was recently shown to promote cell-to-cell spread of *Lm* through its ability to damage the plasma membrane within protrusions⁸. We predicted that ATG16L1-mediated plasma membrane repair might impact cell-to-cell spread by *Lm*.

To test this hypothesis, we examined *Lm* cell-to-cell spread using an infection focus assay⁸. HeLa cells were used as phagosome escape and spread by *Lm* does not require LLO in this cell type⁴⁰. In HeLa cells infected by WT *Lm*, we observed an increase in the size of infection foci after siRNA knockdown of ATG5, ATG12 or ATG16L1 (Fig. 6a,b, and Supplementary Fig. 6a,b and 9). In contrast, cells infected with LLO-deficient *Lm* (Δ hly) did not display differences in spread upon ATG knockdown (Fig. 6a,b). Depletion of ATG3 or ATG9A did not affect *Lm* spread (Supplementary Fig. 6a,b and 9). MEFs deficient in ATG5, ATG12 or ATG16L1 also displayed increased cell-to-cell spread by WT *Lm* (Fig. 6c and Supplementary Fig. 6c). Using mice previously described⁴¹, we found that ATG5 restricts bacterial spread in bone marrow-derived macrophages in vitro (Supplementary Fig. 7), indicating that ATGs can limit *Lm* spread in multiple cell types. Our findings are consistent with a protective role for ATG5 in myeloid cells during *Lm* infection in vivo⁴¹. We conclude that ATG16L1 and its binding partners ATG5 and ATG12 limit LLO-mediated *Lm* spread by a pathway distinct from canonical autophagy.

ATG16L1 Δ CCD MEFs displayed increased *Lm* spread compared to control MEFs, indicating that ATG5-12 binding is

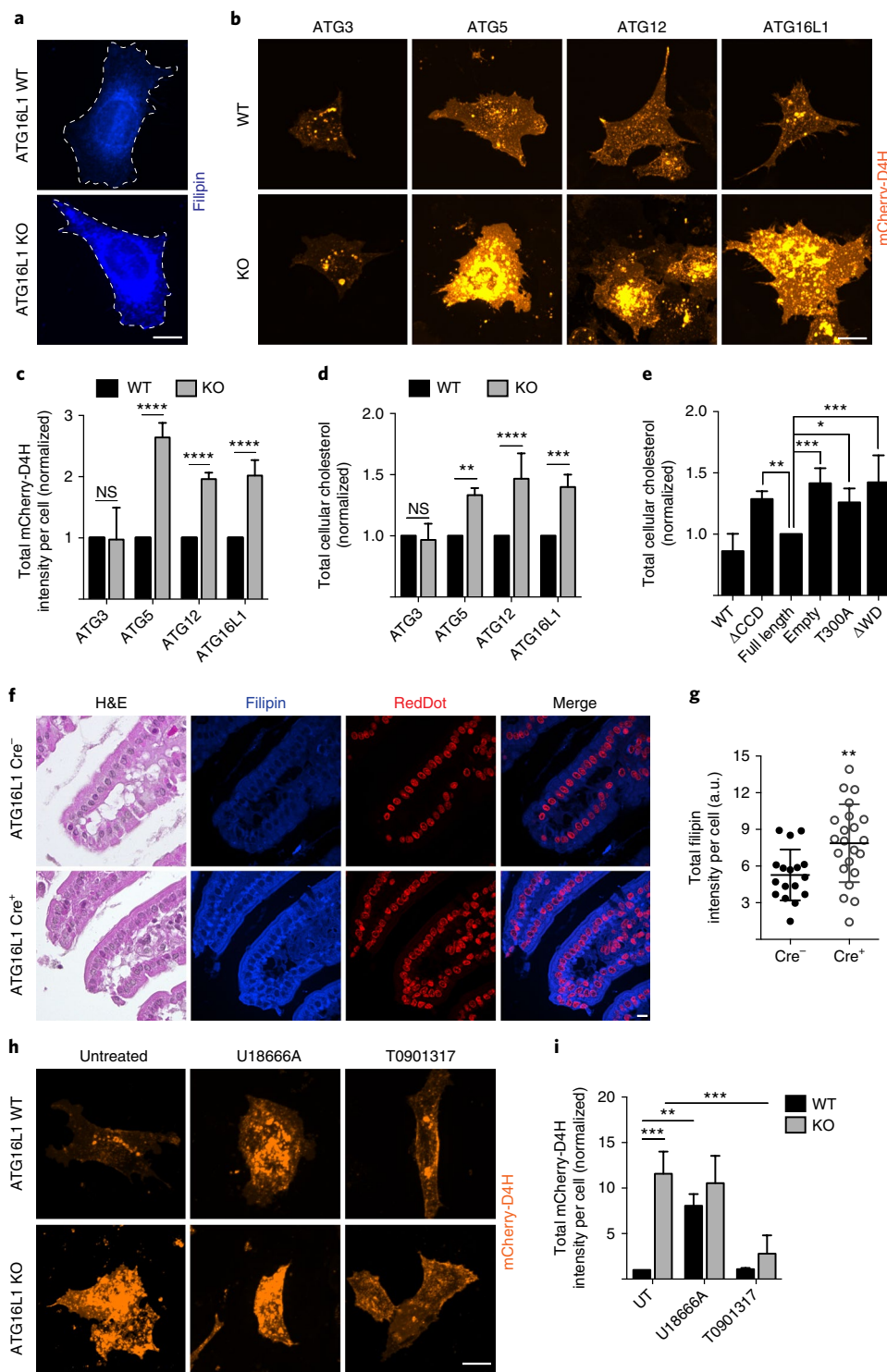


Fig. 4 | ATG16L1 deficiency causes intracellular cholesterol accumulation. **a**, Filipin staining of cholesterol in ATG16L1 WT and KO MEFs. Images are representative of three independent experiments. **b**, Indicated WT and KO MEFs were transfected with mCherry-D4H probe for intracellular cholesterol. Images are representative of three independent experiments. **c**, Fluorescence intensity of transfected mCherry-D4H cells in **(b)** were measured per cell volume ($N=120$ cells). P value was calculated using two-way ANOVA. **d**, Amplex red biochemical assay measuring total cholesterol in the cell from the lysate of indicated WT and KO MEFs ($N > 200,000$ cells). P value was calculated using two-way ANOVA. **e**, Amplex red assay measuring total cholesterol in the cell from the lysate of the indicated mutant ATG16L1 MEFs ($N > 200,000$ cells). P value was calculated using one-way ANOVA. **f**, Small intestines (SI) from ATG16L1^{fllox/fllox} Villin-Cre mice stained with H&E, Filipin and nuclear dye RedDot. Images are representative for six Cre⁺ and seven Cre⁻ mice. **g**, Fluorescence intensity of Filipin in **h** were measured per cell per SI villus ($N=120$ cells). P value was calculated using a two-tailed Mann-Whitney test. **h**, ATG16L1 WT and KO MEFs were transfected with mCherry-D4H and treated with U18666A ($3 \mu\text{g ml}^{-1}$) or T0901317 ($30 \mu\text{M}$). Images are representative for three independent experiments. **i**, Fluorescence intensity of transfected mCherry-D4H ATG16L1 WT and KO MEFs were measured per cell volume ($N=120$ cells). P value was calculated using two-way ANOVA. All data shown as mean \pm s.d. for at least three independent experiments. ** $P < 0.01$, *** $P < 0.001$, **** $P < 0.0001$, NS > 0.9892 . Scale bars, $11 \mu\text{m}$.

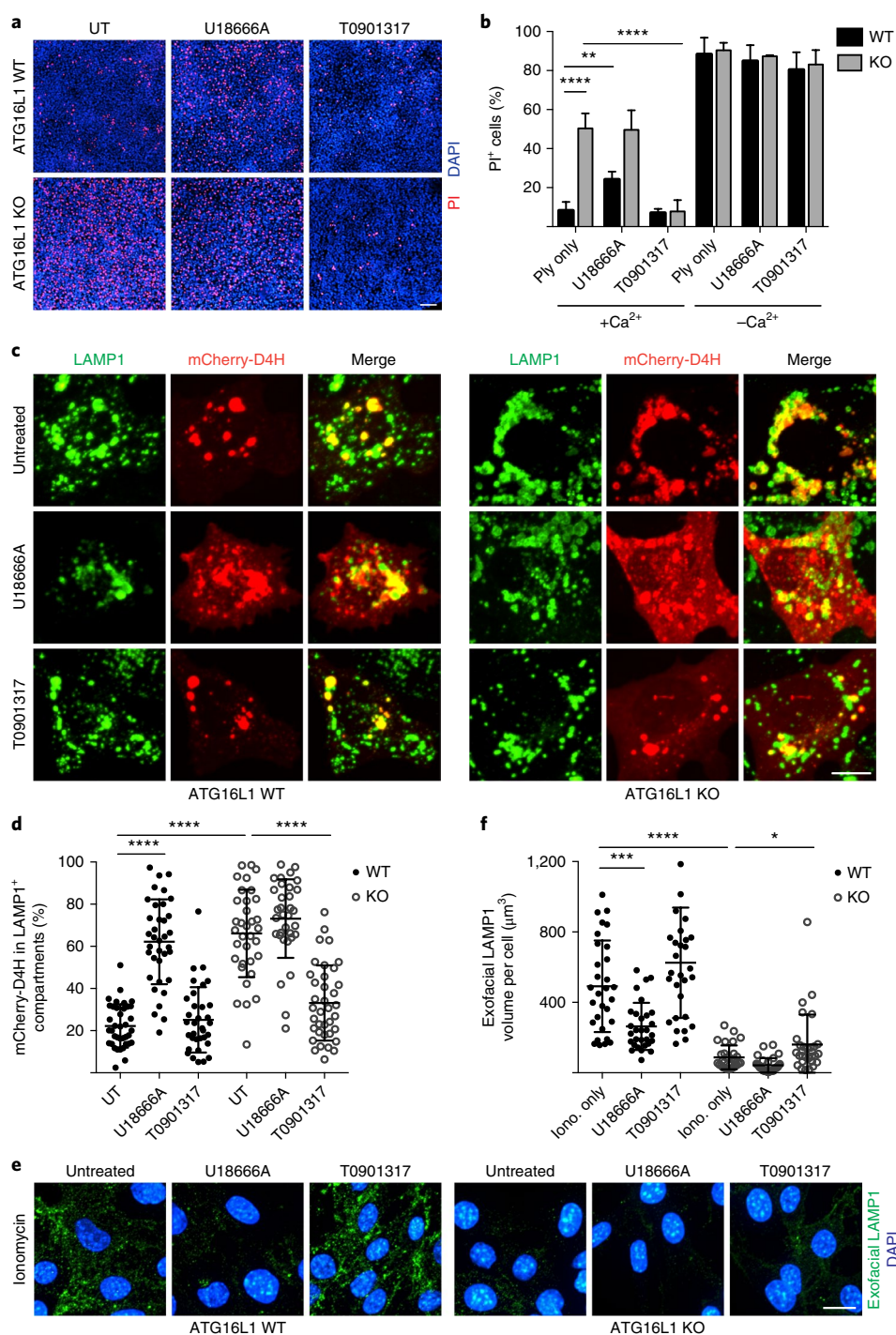


Fig. 5 | Cholesterol accumulation in ATG16L1-deficient cells impairs membrane repair and lysosome exocytosis. **a**, ATG16L1 WT and KO MEFs were subjected to a propidium iodide assay in the presence of U18666A ($3\ \mu\text{g ml}^{-1}$) or T0901317 ($30\ \mu\text{M}$). Images are representative of three independent experiments. Scale bar, $70\ \mu\text{m}$. **b**, Number of PI⁺ cells were enumerated ($N=30,000\text{--}40,000$ cells). P value was calculated using two-way ANOVA. **c**, ATG16L1 WT and KO MEFs were transfected with mCherry-D4H in the presence of U18666A or T0901317 and stained for intracellular lysosome. Images are representative of three independent experiments. Scale bars, $11\ \mu\text{m}$. **d**, Volume of mCherry-D4H in LAMP1 positive compartments per cell was enumerated ($N=90\text{--}120$ cells). P value was calculated using one-way ANOVA. **e**, ATG16L1 WT and KO MEFs were treated with ionomycin ($5\ \mu\text{M}$) to induce lysosome exocytosis, in the presence of U18666A or T0901317. Representative images of exofacial LAMP1 for three independent experiments. Scale bars, $11\ \mu\text{m}$. **f**, Total exofacial LAMP1 volume per cell was enumerated ($N=450$ cells). P value was calculated using one-way ANOVA. All data shown as mean \pm s.d. for three independent experiments. * $P < 0.05$, ** $P < 0.01$, *** $P < 0.001$, **** $P < 0.0001$.

required for ATG16L1's ability to restrict bacterial dissemination (Fig. 6d and Supplementary Fig. 6d). Stable expression of the human full-length ATG16L1, but not the T300A variant or

ΔWD mutant, was sufficient to reduce *Lm* cell-to-cell spread. Thus, expression of the IBD risk allele T300A leads to increased cell-to-cell spread by *Lm*.

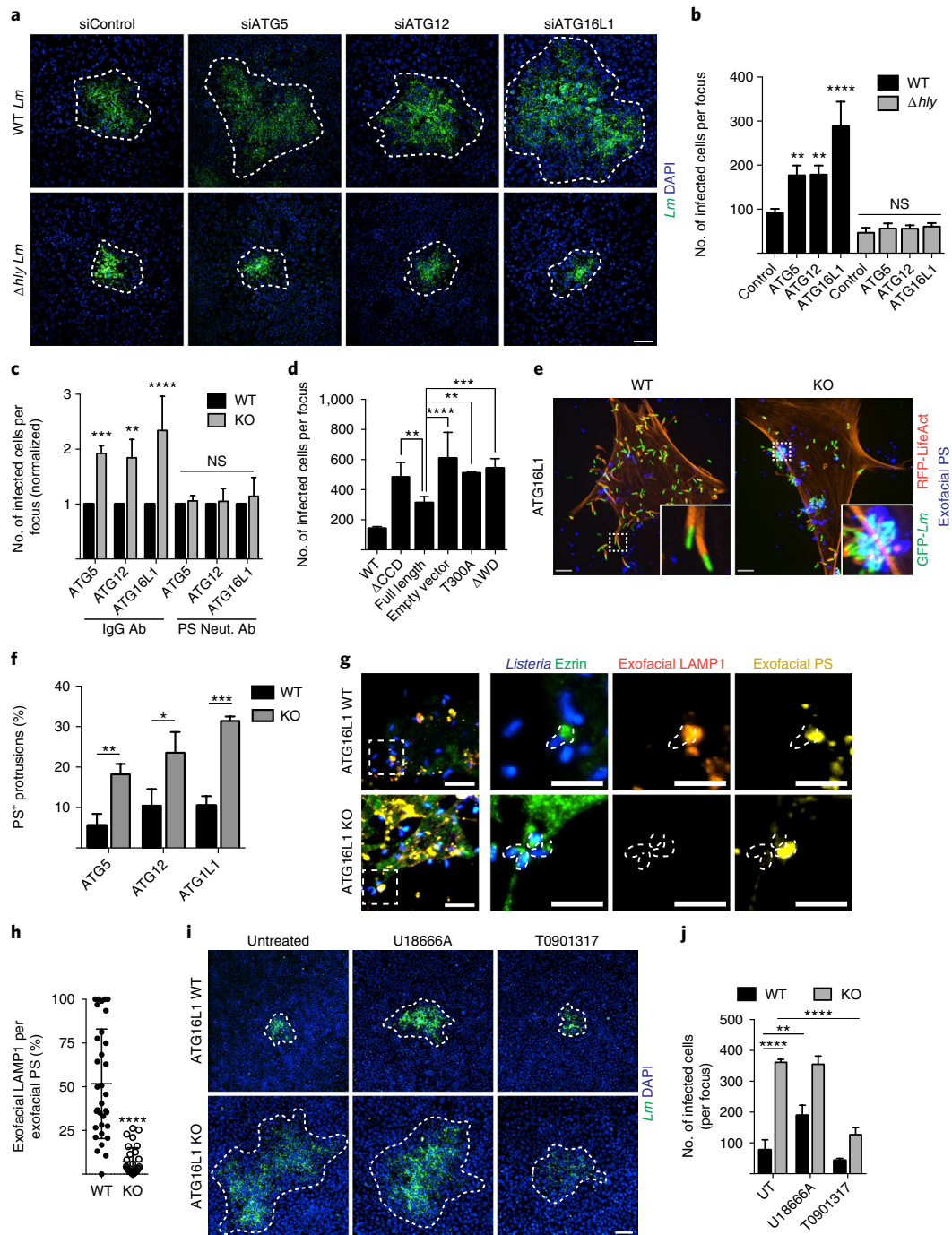


Fig. 6 | ATG16L1 limits cell-to-cell spread of *Lm* by promoting lysosome exocytosis and plasma membrane repair. **a**, Infection focus assay to measure cell-to-cell spread. HeLa cells were transfected with indicated siRNAs and infected with WT and Δhly *Lm*. Dotted lines delineate the edge of the infection foci. Images are representative of three independent experiments. Scale bar, 70 μ m. **b**, Number of infected cells per infection focus were enumerated using DAPI ($N=150$ foci). P value was calculated using one-way ANOVA, NS > 0.9995. **c**, MEFs were infected with *Lm* in the presence of IgG or phosphatidylserine neutralizing antibody. The number of infected cells per focus was measured and shown as normalized means ($N=150$ foci). P value was calculated using two-way ANOVA, NS > 0.9779. **d**, ATG16L1 MEFs with T300A mutation and WD domain deletion were infected with *Lm* ($N=150$ foci). P value was calculated using one-way ANOVA. **e**, Protrusion assay of ATG16L1 WT and KO MEFs. LifeAct-RFP transfected cells were infected with GFP-*Lm* for 7 h. Annexin A5-647 was used to label PS⁺ protrusions (defined as *Lm* away from cell cortex). Insets display protrusions with and without phosphatidylserine labelling. Images are representative of three independent experiments. Scale bars, 11 μ m. **f**, PS⁺ protrusions per cell were quantified ($N=60$ cells). P value was calculated using two-way ANOVA. **g**, Representative images from three independent experiments of exofacial LAMP1 and phosphatidylserine during infection of ATG16L1 WT and KO MEFs with *Lm*. Dotted lines outline bacteria protrusions. Scale bars, 11 μ m. Cropped region scale bars, 5 μ m. **h**, Exofacial LAMP1 signal quantified and normalized to levels of exofacial phosphatidylserine on protrusions ($N=60$ cells). P value was calculated using a two-tailed Mann-Whitney test. **i**, ATG16L1 WT and KO MEFs were infected with *Lm* in the presence of U18666A (1 μ g ml⁻¹) or T0901317 (30 μ M). Images are representative of three independent experiments. Scale bar, 70 μ m. **j**, The number of infected cells per focus was enumerated ($N=150$ foci). P value was calculated using two-way ANOVA. All data shown as mean \pm s.d. for three independent experiments. * $P < 0.05$, ** $P < 0.01$, **** $P < 0.001$, ***** $P < 0.0001$.

It was previously shown that LLO-mediated damage to the plasma membrane causes exposure of exofacial phosphatidylserine on protrusions, promoting bacterial spread via phosphatidylserine-binding receptors on neighbouring cells⁸. Blocking antibodies that target phosphatidylserine impaired bacterial spread in MEFs deficient in ATG5, ATG12 or ATG16L1, indicating that these ATGs limit cell-to-cell spread by reducing exofacial phosphatidylserine exposure (Fig. 6c and Supplementary Fig. 6c). In support of this, we observed an increase in PS⁺ *Lm* protrusions in MEFs deficient in ATG5, ATG12 or ATG16L1 compared to control (Fig. 6e,f). Intracellular bacterial numbers were not affected by loss of ATG5, ATG12 or ATG16L1 in MEFs (Supplementary Fig. 6e). Our findings indicate that ATG16L1 and its binding partners limit cell-to-cell spread by promoting membrane repair and reducing exofacial phosphatidylserine exposure on protrusions.

ATG16L1 promotes lysosomal exocytosis during *Lm* infection. We examined lysosomal exocytosis during *Lm* infection by immunostaining infected cells for exofacial LAMP1 (Fig. 6g,h). We also immunostained total cellular Ezrin, a marker of protrusions induced by *Lm*³⁹. In control MEFs, we observed lysosomal exocytosis associated with Ezrin⁺ protrusions. Similar to Ply-treated cells, infected ATG16L1-deficient MEFs displayed a defect in lysosomal exocytosis (Fig. 6g,h). Thus, ATG16L1 deficiency leads to a localized defect in lysosomal exocytosis at *Lm* protrusions.

Cholesterol accumulation promotes bacterial cell-to-cell spread in ATG16L1-deficient cells. Since our studies suggested that cholesterol accumulation contributed to plasma membrane repair defects in ATG16L1-deficient cells, we examined the role of cholesterol during *Lm* infection. Treatment of cells with U18666A was sufficient to increase cell-to-cell spread of *Lm* in control MEFs, but not ATG16L1-deficient MEFs (Fig. 6i,j). In contrast, T0901317 treatment of ATG16L1-deficient MEFs restricted cell-to-cell spread of *Lm*. Together, these studies suggest that cholesterol accumulation in ATG16L1-deficient cells and its negative impact on lysosomal exocytosis contributes to enhanced cell-to-cell spread of *Lm* during infection.

Discussion

Previous studies have suggested that the plasma membrane can act as a lipid donor for autophagosome biogenesis⁴². Here, we show that components of the autophagy pathway are crucial in maintaining the integrity of the plasma membrane. A previous study by Hagedorn and colleagues indicated that autophagy promotes *Mycobacterium marinum* dissemination by maintaining the integrity of the host cell plasma membrane¹⁷. In their study, ATG8⁺ autophagosomes were found to fuse with the plasma membrane during bacterial ejection from host cells. In contrast, our study reveals a role for ATG16L1 and its binding partners ATG5 and ATG12 in restricting the dissemination of *Lm* within several mammalian cell types. Our finding that RUBICON, ATG3, ATG9 and ATG14 are not required for this phenotype suggests that ATG16L1 acts via a non-canonical pathway. In support of this notion, we did not observe recruitment of ATG16L1 or the ATG8 homologue LC3B to the plasma membrane in response to membrane damage (Supplementary Fig. 1e,f). Therefore, specific components of the autophagy machinery appear to affect distinct pathways to maintain integrity of the plasma membrane during bacterial infection. Previous studies have also demonstrated non-canonical functions of ATG12-ATG3 in late endosome distribution and intraluminal vesicle formation through ESCRT-associated machineries⁴³. Our findings are consistent with an emerging view that autophagy components are involved in many stress pathways, beyond their established role in starvation resistance via canonical autophagy.

ATG16L1 hypomorphic mice are susceptible to alpha-toxin from *Staphylococcus aureus* due to an increase in cell surface expression

of the toxin receptor ADAM-10⁴⁴. Thus, cell autonomous resistance and resilience to different bacterial toxins by ATG16L1 may result from its ability to alter the cell surface proteome and/or promote the plasma membrane repair pathways identified here. We also show that the T300A variant of ATG16L1 has a defect in plasma membrane repair, providing further insight into its role in the pathogenesis of many human diseases²¹⁻²⁵. While other proteins and complexes such as annexins, ESCRTs and calpains function as crucial repair pathways¹¹, we showed that disruption in ATG16L1 alone is sufficient to perturb membrane integrity after exposure to PFTs, which suggests a vital role in rapid plasma membrane repair.

Given the importance of plasma membrane integrity for cell survival, it is not surprising that cells have evolved multiple mechanisms to ensure membrane integrity. Here we show that ATG16L1 is required for efficient cytoprotective blebbing responses during toxin treatment. It is well established that bleb growth and cortical tension are interconnected³³. Whether ATG16L1 affects blebbing directly or indirectly via lysosomal exocytosis to decrease membrane tension remains a subject for future study. Autophagy has many links to lysosome function and cellular growth^{45,46}. Here we show that ATG16L1 is required for lysosomal exocytosis to promote plasma membrane repair upon bacterial pore-forming damage. However, at basal state, ATG16L1 poorly colocalizes with LAMP1 (Supplementary Fig. 5d,e), arguing against a direct effect of ATG16L1 on lysosomes. Instead, the defect of lysosome exocytosis in ATG16L1-deficient cells appears to be partially due to the accumulation of cellular cholesterol, particularly in LAMP1⁺ compartments. Cholesterol accumulation has been linked to plasma membrane repair defects³⁵, possibly caused by changes to the stiffness of the plasma membrane³⁴, or due to defects in the activity of Rab GTPases⁴⁷ and microtubule motors⁴⁸. There are many pathways that regulate cholesterol homeostasis in eukaryotic cells⁴⁹. ATG5 mediates cholesterol efflux from macrophage foam cells by a mechanism that remains unclear³⁶. It is plausible that ATG16L1 plays a role in lipid metabolism by regulating degradation, transport, trafficking or efflux of cholesterol to and from the lysosome, ultimately affecting membrane repair. The mechanism by which ATG16L1 deficiency leads to cholesterol accumulation will be an important topic for further study.

Autophagy can target intracellular bacteria and limit their growth in host tissues⁷. Certain pathogens such as *Lm* have evolved virulence strategies to evade autophagy in host cells¹⁵. Indeed, ATG5 deficiency in macrophages has no effect on intracellular growth of *Lm* in bone marrow-derived macrophages in vitro⁵⁰. However, mice deficient in haematopoietic ATG5 expression display increased susceptibility to systemic *Lm* infection⁴¹. Our findings suggest that ATG5-mediated limitation of cell-to-cell spread by *Lm* might contribute to the in vivo phenotype of ATG5 deficiency in mice, which may involve factors beyond membrane repair. Importantly, our findings reveal that autophagy components (but not autophagy per se) restrict *Lm* spread through their impact on plasma membrane repair. In summary, our study identifies ATG16L1 as an important factor in cholesterol regulation in lysosomes and plasma membrane repair that acts as an innate immune defence by limiting pathogen dissemination during infection.

Methods

Bacterial strains and toxins. *Lm* were grown in brain-heart infusion broth and the following strains were used: 10403S (WT)⁵¹, DP-L2161 (Δhly)⁵², DP-L3078 ($\Delta actA$)⁵³. WT *Lm* 10403S expressing GFP under the *hly* promoter (DP-L1039) was previously described⁵⁴. Ply⁵⁵ was a gift from A. Ratner. EGFP-Ply⁵⁶ was a gift from A. Draeger.

Antibodies, constructs and reagents. Primary antibodies (1:100) used were rabbit anti-*Listeria* (#B223021 from BD Biosciences), mouse anti-ezrin (#35-7300 from Invitrogen) and rat anti-mouse LAMP1 (1D4B was deposited to the Developmental Studies Hybridoma Bank by J.T. August). The following primary

antibodies used were from Cell Signaling: ATG3 (#3415S), ATG5 (#2630), ATG9A (#13509S), ATG12 (#2010), ATG16L1 (#8089S). Anti-phosphatidylserine neutralizing antibody (Abcam #18005) and IgG isotype control (Biolegend #400401) were used at 1:200 dilution. Alexa Fluor-568 Phalloidin, annexin A5 Alexa Fluor-488, -568 and -647 conjugates and all fluorescent secondary antibodies (Alexa Fluor conjugates) were from Invitrogen. Filipin III (#F4767) was from Sigma. 4,6-Diamidino-2-phenylindole (DAPI) (#D1306 Invitrogen) and RedDot2 (Biotium 200 \times , #40061) were used at 1:2,500 dilution and 1 \times respectively to stain the nuclei where indicated. Blebbistatin (#B0560; 100 μ M final), T0901317 (#T2320; 20–30 μ M final) and ionomycin (#I3909, 5 μ M) were from Sigma, U18666A (#10009085; 1–3 μ g ml⁻¹ final) was from Cayman Chemical, Calyculin A (#208851; 20 μ M final) was from Millipore. For transfection of HeLa and MEF cells, Xtreme Gene 9 (Roche) and GeneJuice (Millipore) transfection reagents were used as per manufacturer's protocols. The following constructs were obtained as gifts: Annexin-A1-GFP⁵⁷ (V. Gerke), Annexin-A2-GFP and Annexin-A6-YFP (A. Draeger), LC3-GFP⁵⁸ (T. Yoshimori), ATG16L1-mStrawberry⁵⁹ (D. Rubinsztein), LifeAct-mRFP⁶⁰ (R. Truant), GFP-LAMP1 (J.-P. Gorvel), HIS6X-GFP-D4 and mCherry-D4H constructs were previously described²⁸. The following siRNAs were purchased from Sigma: ATG3 (#0022874), ATG5 (#00173156), ATG9A (#00312184), ATG12 (#00161609), ATG16L1 (#00351011).

Cell culture and macrophage generation. HeLa and MEF cells were cultured in DMEM (Hyclone) supplemented with 10% heat-inactivated FBS (Wisent) without antibiotics at 37 °C and 5% CO₂. All cells used were authenticated and tested negative for mycoplasma by ATCC and The Hospital for Sick Children Biobank. The following KO HeLa and MEFs and their corresponding control cell lines were obtained from: ATG16L1 (R. Xavier), ATG3 and ATG12 (J. Debnath), RUBICON, ATG3 (HeLa), ATG5, ATG9, ATG14, ATG16L1 (HeLa), ATG16L1 T300A mutant and Δ WD repeat domain (T. Yoshimori). HeLa-CHMP4B-GFP³⁰ was a gift from MPI-CPG. All experimental protocols involving mice were approved by the Animal Care Committee of The Hospital for Sick Children. Mice were euthanized by CO₂ inhalation. Mouse BMDMs were obtained from the dissected femurs and tibias of 6–8-week-old male C57BL/6 mice. Cells were washed with growth medium and plated on 70 cm² Petri dishes. Medium was replaced every 2 days and after 7–9 days cells were used for experiments. Cells were maintained in high-glucose RPMI-1640 medium (Wisent #350-025-CL) containing 10% heat-inactivated FBS (Wisent), 1% sodium pyruvate (Wisent), 1% non-essential amino acids (Wisent), 0.5% 2-mercaptoethanol (Gibco), 1% penicillin and streptomycin (Invitrogen), and 10% L929 medium. L929 medium was generated by growing a confluent layer of L929 cells in 175 cm² flasks in DMEM supplemented with 10% heat-inactivated FBS. When cells reached confluency, growth medium was replaced by DMEM alone. After 7 days, supernatant was collected, centrifuged, filtered and stored at –20 °C.

Propidium iodide assay of membrane integrity. ATG WT and KO MEF and HeLa cells were plated at 4 \times 10⁵ cells and 5 \times 10⁵ cells per well respectively in 24-well tissue culture plates with glass coverslips 24 h and 72 h before toxin treatment. Where indicated, HeLa cells were transfected with siRNAs after 18 h and the media was changed 24 h later. Cells were treated with either 200 ng ml⁻¹ (MEF) or 100 ng ml⁻¹ (HeLa) Ply, or 0.004% (v/v) digitonin diluted in Tyrode's buffer (10 mM HEPES, 10 mM glucose, 5 mM potassium chloride, 140 mM sodium chloride, 1 mM EGTA, 1 mM magnesium chloride, 2 mM calcium chloride, pH 7.4) for 20 min at 37 °C, and cells were washed with PBS with or without calcium and magnesium (PBS⁺, Wisent #311-420-CL; PBS⁻, Wisent #311-010-CL), and subsequently replaced with Tyrode's buffer with or without calcium for 10 min. For Tyrode's buffer lacking calcium, the 2 mM calcium chloride was replaced with 2 mM magnesium chloride. Cells were then incubated with 0.4 mg ml⁻¹ propidium iodide (Sigma #P4170) in either Tyrode's buffer with or without calcium for 10 min. Cells were fixed with 2.5% PFA (EM Sciences #15710), counterstained with DAPI, and imaged on a Quorum spinning disk confocal scan head (Leica DMI 6000 B inverted fluorescence microscope, Hamamatsu ORCA Flash 4 sCMOS and colour camera) equipped with a \times 10 objective. PI⁺ cells were quantified using Velocity 6 software.

Immunofluorescence. Immunostaining was conducted as previously described⁸. Briefly, cells were permeabilized and blocked in PBS⁺ containing 0.2% saponin (Calbiochem) and 10% normal goat serum (SS-PBS) for 30 min. Subsequently cells were incubated for 1 h with primary antibodies in SS-PBS. Cells were washed three times with PBS⁺ and incubated with secondary Alexa Fluor conjugated antibodies for 1 h. Cells were washed three times with PBS⁺, mounted in fluorescence mounting medium (Dako). Confocal images were imported into Adobe Photoshop and assembled in Adobe Illustrator for labelling.

Ply titration assay. MEF cells were plated at 4 \times 10⁵ cells per well in 24-well tissue culture plates 24 h before toxin treatment. Cells were treated with 5 to 200 ng ml⁻¹ Ply diluted in Tyrode's buffer without calcium for 5 min at 37 °C. Cells were washed with PBS⁻ and replaced with Tyrode's buffer without calcium containing 0.4 mg ml⁻¹ propidium iodide for 10 min. Cells were fixed with 2.5% PFA and counterstained with DAPI, and imaged on a Quorum spinning disk confocal microscope equipped with a \times 10 objective.

Ply binding assay. MEF cells were plated at 2 \times 10⁵ cells per well in 6-well tissue culture plates 24 h before toxin treatment. Cells were treated with 100 ng ml⁻¹ EGFP-Ply diluted in Tyrode's buffer without calcium for 5 min at 4 °C. Cells were washed with PBS⁻, trypsinized and resuspended in PBS⁻ with 0.1% FBS. Samples were analysed using a Becton Dickinson flow cytometer, gated using negative unstained control cells and quantified on FlowJo software (Version 10).

Flow cytometry assay of membrane repair. ATG16L1 MEFs and HeLa cells were plated at 7.5 \times 10⁴ cells per well in 6-well tissue culture plates 48 h and 72 h, respectively, before toxin treatment. Control and ATG12 siRNAs were applied to HeLa cells after 18 h and the media was changed 24 h later. Cells were pulsed with Ply toxin (100 ng ml⁻¹) for 10 min. Cells were washed with PBS⁺ and replaced with Tyrode's buffer with calcium containing 5 μ g ml⁻¹ propidium iodide and chase at the indicated times. Cells were washed with PBS⁻, trypsinized and resuspended in PBS⁻ with 0.1% FBS. Samples were collected and analysed on a Becton Dickinson flow cytometer, gated using negative unstained control, and quantified on FlowJo software.

Cholesterol binding assay. MEF cells were plated at 2 \times 10⁵ cells per well in 6-well tissue culture plates 24 h before cholesterol probe treatment. Cells were treated with 150 μ g ml⁻¹ HIS6X-GFP-D4 diluted in ice-cold Tyrode's buffer without calcium for 10 min at 4 °C. Cells were washed with PBS⁻, scraped and resuspended in PBS⁻ with 0.1% FBS. Samples were analysed using a Becton Dickinson flow cytometer (LSR II), gated using negative unstained control cells, and quantified on FlowJo software.

Flow cytometry assay of mechanical scrape wounding. ATG16L1 WT and KO MEFs were plated at 1 \times 10⁵ cells per well in 6-well tissue culture plates 48 h before scrape wounding. Cells were washed twice with warm Tyrode's buffer with or without calcium, and mechanically damaged by rapidly scraping 12 times with a 17 mm blade cell scraper (Sarstedt) using the same pattern. The resuspended cells were incubated at 37 °C for 5 min to allow for repair. Tyrode's buffer with or without calcium containing 5 μ g ml⁻¹ propidium iodide was then added to the cell and incubated for an additional 5 min at 37 °C. Cells were placed on ice, washed with cold PBS⁺ and resuspended in cold PBS⁺ with 0.1% FBS. Samples were collected and analysed on a Becton Dickinson flow cytometer, quantified on FlowJo software, and gated using negative unstained control. The mechanical wounding assay by scraping cells was previously described³².

Lysosomal exocytosis upon Ply treatment. MEF cells were plated at 8 \times 10³ cells per well onto 96-well glass bottom plates (Greiner) 24 h before toxin treatment. Cells were treated with 166 ng ml⁻¹ Ply in Tyrode's buffer with calcium for 10 min at 37 °C. Where indicated, cells were incubated with T0901317 (30 μ M) and U18666A (3 μ g ml⁻¹) 4 h and 24 h respectively prior to Ply-induced damage to assess the role of cholesterol in lysosomal exocytosis. To visualize exofacial LAMP1, cells were washed with ice-cold PBS⁺ and then incubated in PBS⁺ containing 10% goat serum for 30 min on ice with 1% (v/v) monoclonal antibody (1D4B) that recognizes a luminal sequence of the LAMP1 protein. In parallel, cells were also labelled with 1% (v/v) annexin A5 Alexa Fluor-568 conjugate to visualize exofacial phosphatidylserine. Cells were then washed with PBS⁺ and fixed with 4% PFA for 15 min at room temperature (RT). For total LAMP1 staining, cells were permeabilized and blocked in SS-PBS for 30 min and incubated with LAMP1 antibody for 1 h. Cells were washed three times with PBS⁺ and incubated with secondary anti-rat Alexa Fluor-488 conjugated antibodies for 1 h. Cells were counterstained with DAPI and kept in PBS⁺. Twenty-three z-stack images were acquired at 0.5 μ m step size using a spinning disk confocal microscope equipped with a \times 63 objective. For exofacial LAMP1, Velocity 6 software was used to quantify the volume of exofacial LAMP1 per cell (percentage of LAMP1⁺ volume per nuclei) or normalized to the volume of exofacial phosphatidylserine (percentage of LAMP1⁺ volume per Annexin A5⁺ volume) using an intensity threshold of 1500 (a.u.). For total LAMP1, the volume of total LAMP1 per cell (percentage of LAMP1⁺ volume per nuclei) and the intensity of total LAMP1 per cell (LAMP1⁺ intensity per nuclei) were quantified. LAMP1 exocytosis assay was previously described³².

Live cell imaging of bleb formation. MEF cells were plated at 1 \times 10⁵ cells per well in 6-well tissue culture plates with glass coverslips 48 h before experiment. Serum-free DMEM medium containing 20 μ M CellTracker Green was added to the culture 2 h before imaging. After 30 min incubation, cells were washed three times with PBS and DMEM medium containing 10% FBS was added. Then 40 min and 50 min before imaging, cells were treated with Calyculin A (20 μ M) and Blebbistatin (100 μ M) respectively. Coverslips were transferred to imaging chambers containing live cell imaging media, 200 ng ml⁻¹ Ply and 1% (v/v) Annexin A5 Alexa Fluor 647 (Invitrogen). Cells were imaged at 37 °C using a spinning disk confocal microscope equipped with a \times 63 objective. Images were taken at 20 μ m z-stacks with a 0.5 μ m step every 60 sec for 15 min.

Propidium iodide assay with pharmacological treatments. MEF cells were plated at 4 \times 10⁵ cells per well in 24-well tissue culture plates with glass coverslips

24 h before experiment. Then 40 min and 50 min before toxin treatment, cells were treated with Calyculin A (20 μM) and Blebbistatin (100 μM), respectively. Cells were treated with 200 ng ml^{-1} Ply diluted in Tyrode's buffer with calcium for 20 min at 37 $^{\circ}\text{C}$, and cells were washed with PBS with and without calcium and magnesium, and subsequently replaced with Tyrode's buffer with or without calcium for 10 min. Cells were then incubated with 0.4 mg ml^{-1} propidium iodide (Sigma) in either Tyrode's buffer with or without calcium for 10 min. Cells were fixed with 2.5% PFA and counterstained with DAPI, and imaged on a Quorum spinning disk confocal scan head equipped with a $\times 10$ objective. PI⁺ cells were quantified using Volocity 6 software.

Atomic force microscopy. MEF cells were plated at 1×10^5 cells per Willco dishes (64–0759, Warner Instruments). All force–distance curves were collected using a Digital Instruments Bioscope scanning probe system and a Digital Instruments Nanoscope IIIA controller with software version 5.30r3sr3. The Bioscope system was mounted onto an Olympus IX-70 inverted microscope base equipped for both confocal and total internal reflection fluorescence (TIRF) imaging. Regions of interest for the force spectroscopy experiments were identified optically using a $\times 60$ objective (PlanApo, Olympus) and the atomic force microscopy tip centred in the optical field of view. The force curves were acquired using DNP-10 D-tips (nominal spring constant of 0.06 N m^{-1} and nominal tip radius of 20 nm) previously irradiated with ultraviolet light for 15 min. The tips were calibrated for deflection sensitivity on cell-free region of the Willco dishes. The tip was positioned at the midpoint between the edge and the nucleus of the cells. All cells were stained with cell tracker to assist with tip positioning. To prevent cell damage, the tip was raised at least 30 μm above the Willco dish surface before initiating the force spectroscopy experiments. Force spectra were acquired by stepping the tip towards the surface in 1 μm increments and, at each step, collecting a single force curve cycle using a ramp size of 1 mm at a tip scan rate of 1 Hz corresponding to a tip velocity of 1 mm s^{-1} . Relative trigger mode was used to avoid possible system drifts due to mechanical causes or thermal effects that increase total applied force. A range of trigger loads from 0.5 to 3 nN was considered. All analyses were performed on force curves collected with a trigger force of 3 nN. The data collection for each Willco dish took less than 1.5 h to ensure the health and mobility of the cells. Young's modulus values were determined after processing the approach curves (150 nm indentation post contact point) using Indentation Analysis in Nanoscope Analysis software version 1.40 R3Sr5.96909 with linear fit, tip half angle of 18.00, Poisson's ratio of 0.50 and Sneddon model for conical tip.

Biochemical amplex red cholesterol assay. ATG WT, KO and T300A mutant MEF cells were plated at 5×10^4 cells per well in 6-well tissue culture plates 48 h before cholesterol measurements. Cells were washed with 1 ml cold PBS and lysed with 120 μl of lysis buffer (50 mM Tris-HCl, 150 mM NaCl, 1 mM EDTA, 1% TritonX-100) containing protease inhibitors (NaV, NaF, PMSF, Pepstatin, Leupeptin, Aprotinin). Protein concentration was determined using Pierce BCA protein assay kit (ThermoFisher, #23225). Cellular cholesterol was measured using Amplex Red Cholesterol Assay Kit (Invitrogen, A12216) using manufacturer's recommendations. In brief, 50 μl of cell extract was added to 50 μl of 300 μM Amplex Red Reagent (2 U ml^{-1} horseradish peroxidase, 2 U ml^{-1} cholesterol oxidase and 0.2 U ml^{-1} cholesterol esterase) and incubated at 37 $^{\circ}\text{C}$ for 30 min and protected from the light. The fluorescence was measured after 30 min using Epoch Biotek plate reader. Cellular cholesterol was normalized to protein concentration.

Cholesterol visualization using filipin. ATG16L1 WT and KO MEFs were plated at 1×10^4 cells per well in 24-well tissue culture plates with glass coverslips 48 h before staining. Cells were fixed with 2.5% PFA and stained with 0.01 $\mu\text{g ml}^{-1}$ of filipin III (Sigma) for 16 h. Cells were imaged on Quorum spinning disk confocal scan head equipped with a $\times 63$ objective.

Propidium iodide assay with cholesterol drugs. ATG WT and KO MEF cells were plated at 1×10^5 cells per well in 24-well tissue culture plates with glass coverslips 48 h before toxin treatment. Cells were incubated with T0901317 (30 μM) or U18666A (3 $\mu\text{g ml}^{-1}$) 4 h and 24 h respectively, prior to toxin treatment. Cells were treated with 200 ng ml^{-1} Ply diluted in Tyrode's buffer with calcium for 10 min at 37 $^{\circ}\text{C}$, and cells were washed with PBS with or without calcium and magnesium, and subsequently replaced with Tyrode's buffer with or without calcium for 10 min. Cells were then incubated with 0.4 mg ml^{-1} propidium iodide in either Tyrode's buffer with or without calcium for 10 min. Cells were fixed with 2.5% PFA, counterstained with DAPI, and imaged on a Quorum spinning disk confocal scan head equipped with a $\times 10$ objective. PI⁺ cells were quantified using Volocity 6 software.

Cholesterol accumulation in lysosomes. ATG WT and KO MEF and HeLa cells were plated at 2.5×10^4 cells and 1×10^4 cells per well in 24-well tissue culture plates with glass coverslips for 48 h and 72 h, respectively. Where indicated, HeLa cells were transfected with siRNAs after 18 h and the media was changed 24 h later. Cells were then transfected with mCherry-D4H probe. This probe encodes an mCherry fusion to the cholesterol-binding domain of the bacterial toxin perfringolysin O, and has been mutated to enhance its sensitivity for cholesterol and to prevent toxin

oligomerization and membrane damage²⁸. Cells were incubated with T0901317 (30 μM) or U18666A (3 $\mu\text{g ml}^{-1}$) 4 h and 24 h, respectively, prior to fixation. Cells were fixed with 2.5% PFA and stained for intracellular LAMP1 as previously described. Cells were imaged on a Quorum spinning disk confocal scan head equipped with a $\times 63$ objective. mCherry-D4H in LAMP1⁺ compartments were quantified using Volocity 6 software.

Mouse intestine staining. Small intestines (SI) were obtained from ATG16L1^{fllox/flox} Villin-Cre mice³¹, flushed with ice-cold PBS and fixed with 10% formalin for 48 h. Tissues were subsequently dehydrated and embedded in paraffin using Leica Tissue Processor (TP 1020) and cassette (Leica, #3802690) in the following series; 70% EtOH (2 h), 95% EtOH (2 h), 100% EtOH (2 h $\times 2$), 100% EtOH (1.5 h $\times 2$), Xylene (1.5 h $\times 2$), Xylene (1 h $\times 2$), paraffin (3 h $\times 4$). Then 4 μm serial cross-sections of SI were obtained using a Leica microtome (RM 2235) and mounted on VWR microslides (#48311-703). Prior to staining, tissue sections were rehydrated in the following series: Xylene (5 min $\times 2$), 100% EtOH (3 min $\times 2$), 95% EtOH (3 min $\times 2$), 75% EtOH (3 min), ddH₂O (rinse). SI were incubated with 100 $\mu\text{g ml}^{-1}$ filipin III (Sigma) diluted in PBS⁺ for 2 h at room temperature, and counterstained with 1X nuclear dye RedDot2 (Biotium). SI was imaged on a Quorum spinning disk confocal scan head equipped with a $\times 63$ objective. Filipin staining was quantified using Volocity 6 software.

Lysosomal exocytosis upon ionomycin treatment. MEF cells were plated at 8×10^3 cells per well onto 96-well glass bottom plates (Greiner) 24 h before treatment. Cells were treated with 5 μM ionomycin in Tyrode's buffer with calcium for 5 min at 37 $^{\circ}\text{C}$. Where indicated, cells were incubated with T0901317 (30 μM) or U18666A (3 $\mu\text{g ml}^{-1}$) 4 h and 24 h, respectively, prior to ionomycin-induced Ca²⁺ influx to assess the role of cholesterol in lysosomal exocytosis. To visualize exofacial LAMP1, cells were washed with ice-cold PBS⁺ and then incubated in PBS⁺ containing 10% goat serum for 30 min on ice with 1% (v/v) monoclonal antibody (1D4B) that recognizes a luminal sequence of the LAMP1 protein. Cells were then washed with PBS⁺ and fixed with 4% PFA for 15 min at room temperature. Cells were counterstained with DAPI and kept in PBS⁺. Twenty-three z-stack images were acquired at 0.5 μm step size using a spinning disk confocal microscope equipped with a $\times 63$ objective. For exofacial LAMP1, Volocity 6 software was used to quantify the volume of exofacial LAMP1 per cell (percentage of LAMP1⁺ volume per nuclei) using an intensity threshold of 500 (a.u.).

Lm infection focus assay. HeLa and MEF cells were plated at 4×10^5 cells per well in 24-well tissue culture plates with glass coverslips 72 h and 24 h before infection, respectively. HeLa cells were transfected with ATG5, ATG12 and ATG16L1 siRNA after 18 h and media was changed 24 h later. MEF cells were infected with WT *Lm* at an MOI of 0.5 in DMEM, and HeLa cells were infected with WT and Δhly mutant bacteria at an MOI of 0.1 in DMEM. Following infection, ATG16L1 WT and KO MEF cells were incubated with DMEM containing 10% FBS in the presence of anti-phosphatidylserine neutralizing antibody (Abcam) and IgG isotype control (Biolegend) thereafter where indicated. At 60 min post-infection, all cells were washed three times with PBS⁺ and cultured in DMEM medium containing 10% FBS and 50 $\mu\text{g ml}^{-1}$ gentamicin (Wisent #400-130-IG). At 18 h post-infection, cells were fixed with 2.5% PFA and counterstained with *Lm* and DAPI, and imaged on a Quorum spinning disk confocal scan head equipped with a $\times 10$ objective. The number of infected cells per focus of infection was quantified using Volocity 6 software.

Live cell imaging of Lm protrusion formation. MEF cells were plated at 5×10^4 cells per well in 6-well tissue culture plates with glass coverslips 48 h before experiment and 24 h prior to infection, cells were transfected with LifeAct-RFP. MEF cells were then infected with WT *Lm* expressing GFP (DP-1039) at an MOI of 100 in DMEM. After 60 min of infection at 37 $^{\circ}\text{C}$, cells were washed three times with PBS⁺ followed by the addition of growth media containing 50 $\mu\text{g ml}^{-1}$ gentamicin. At 6 h post-infection, coverslips were washed with PBS⁺ and transferred into microscope chambers with live cell imaging medium containing 50 $\mu\text{g ml}^{-1}$ gentamicin and 1% (v/v) annexin A5 Alexa Fluor 647 conjugate (Invitrogen). MEF cells were maintained at 37 $^{\circ}\text{C}$ and imaged on a Quorum spinning disk confocal scan head equipped with a $\times 63$ objective. Phosphatidylserine-positive *Lm* protrusions were defined as bacteria above the plane of the cell surface on z-stack slices, and quantified using Volocity 6 software.

Lysosomal exocytosis during Lm infection. MEF cells were plated at 4×10^5 cells per well in 24-well tissue culture plates with glass coverslips 24 h before infection. MEF cells were infected with WT *Lm* at an MOI of 100 in DMEM. After 60 min of infection at 37 $^{\circ}\text{C}$, cells were washed three times with PBS⁺ followed by the addition of growth media containing 50 $\mu\text{g ml}^{-1}$ gentamicin. At 6 h post-infection, cells were washed with ice-cold PBS⁺ and then incubated in PBS⁺ containing 10% goat serum for 30 min on ice with 1% (v/v) LAMP1 antibody. In parallel, cells were also labelled with 1% (v/v) annexin A5 Alexa Fluor 647 conjugate to visualize exofacial phosphatidylserine. Cells were then washed with PBS⁺ and fixed with 4% PFA for 15 min at RT. To visualize protrusions, cells were stained with antibodies to *Lm* and ezrin, and imaged on a Quorum spinning disk confocal scan head equipped with a

×63 objective. Exofacial LAMP1 and exofacial phosphatidylserine were quantified using Volocity 6 software.

Infection focus assay with cholesterol drugs. ATG16L1 WT and KO MEF cells were plated at 1×10^5 cells per well in 24-well tissue culture plates with glass coverslips 24 h before infection. Throughout the infection time course, cells were incubated with T0901317 (30 μM) or U18666A (1 $\mu\text{g ml}^{-1}$). MEF cells were infected with WT *Lm* at an MOI of 0.5 in DMEM. At 60 min post-infection, all cells were washed three times with PBS⁺ and cultured in DMEM medium containing 10% FBS and 50 $\mu\text{g ml}^{-1}$ gentamicin. At 18 h post-infection, cells were fixed with 2.5% PFA and counterstained with *Lm* and DAPI, and imaged on a Quorum spinning disk confocal scan head equipped with a ×10 objective. The number of infected cells per focus of infection was quantified using Volocity 6 software.

Statistical analysis. Statistical analyses were conducted using GraphPad Prism v.6.0. The average \pm s.d. is shown in figures, and *P* values were calculated as described in figure legends. *P* < 0.05 was considered statistically significant.

Reporting Summary. Further information on research design is available in the Nature Research Reporting Summary linked to this article.

Data availability

The data that support the findings of this study are available from the corresponding author upon request.

Received: 2 January 2018; Accepted: 12 October 2018;
Published online: 26 November 2018

References

- Dal Peraro, M. & van der Goot, F. G. Pore-forming toxins: ancient, but never really out of fashion. *Nat. Rev. Microbiol.* **14**, 77–92 (2016).
- Babiychuk, E. B. & Draeger, A. Defying death: cellular survival strategies following plasmalemmal injury by bacterial toxins. *Semin. Cell. Dev. Biol.* **45**, 39–47 (2015).
- Cassidy, S. K. & O’Riordan, M. X. More than a pore: the cellular response to cholesterol-dependent cytolytins. *Toxins (Basel)* **5**, 618–636 (2013).
- Osborne, S. E. & Brumell, J. H. Listeriolysin O: from bazooka to Swiss army knife. *Philos. Trans. R. Soc. Lond. B Biol. Sci.* **372**, 20160222 (2017).
- Birmingham, C. L. et al. Listeriolysin O allows *Listeria monocytogenes* replication in macrophage vacuoles. *Nature* **451**, 350–354 (2008).
- Beauregard, K. E., Lee, K. D., Collier, R. J. & Swanson, J. A. pH-dependent perforation of macrophage phagosomes by listeriolysin O from *Listeria monocytogenes*. *J. Exp. Med.* **186**, 1159–1163 (1997).
- Lebreton, A., Stavru, F. & Corsart, P. Organelle targeting during bacterial infection: insights from *Listeria*. *Trends. Cell Biol.* **25**, 330–338 (2015).
- Czuczman, M. A. et al. *Listeria monocytogenes* exploits efferocytosis to promote cell-to-cell spread. *Nature* **509**, 230–234 (2014).
- Cassidy, S. K. et al. Membrane damage during *Listeria monocytogenes* infection triggers a caspase-7 dependent cytoprotective response. *PLoS Pathog.* **8**, e1002628 (2012).
- Pasternak, C. A. Effect of pore formers on intracellular calcium. *Cell Calcium* **7**, 387–397 (1986).
- Jimenez, A. J. & Perez, F. Plasma membrane repair: the adaptable cell life-insurance. *Curr. Opin. Cell Biol.* **47**, 99–107 (2017).
- Babiychuk, E. B., Monastyrskaya, K., Potez, S. & Draeger, A. Blebbing confers resistance against cell lysis. *Cell Death Differ.* **18**, 80–89 (2011).
- Hagmann, J., Burger, M. M. & Dagan, D. Regulation of plasma membrane blebbing by the cytoskeleton. *J. Cell. Biochem.* **73**, 488–499 (1999).
- Roy, D. et al. A process for controlling intracellular bacterial infections induced by membrane injury. *Science* **304**, 1515–1518 (2004).
- Levine, B., Mizushima, N. & Virgin, H. W. Autophagy in immunity and inflammation. *Nature* **469**, 323–335 (2011).
- Ktistakis, N. T. & Tooze, S. A. Digesting the expanding mechanisms of autophagy. *Trends. Cell Biol.* **26**, 624–635 (2016).
- Gerstenmaier, L. et al. The autophagic machinery ensures nonlytic transmission of mycobacteria. *Proc. Natl Acad. Sci. USA* **112**, E687–E692 (2015).
- Gonzalez, M. R. et al. Pore-forming toxins induce multiple cellular responses promoting survival. *Cell Microbiol.* **13**, 1026–1043 (2011).
- Marchiando, A. M. et al. A deficiency in the autophagy gene Atg16L1 enhances resistance to enteric bacterial infection. *Cell. Host. Microbe.* **14**, 216–224 (2013).
- Fadeel, B. & Xue, D. The ins and outs of phospholipid asymmetry in the plasma membrane: roles in health and disease. *Crit. Rev. Biochem. Mol. Biol.* **44**, 264–277 (2009).
- Hampe, J. et al. A genome-wide association scan of nonsynonymous SNPs identifies a susceptibility variant for Crohn disease in ATG16L1. *Nat. Genet.* **39**, 207–211 (2007).
- Kuballa, P., Huett, A., Rioux, J. D., Daly, M. J. & Xavier, R. J. Impaired autophagy of an intracellular pathogen induced by a Crohn’s disease associated ATG16L1 variant. *PLoS ONE* **3**, e3391 (2008).
- Raju, D. et al. Vacuolating cytotoxin and variants in Atg16L1 that disrupt autophagy promote *Helicobacter pylori* infection in humans. *Gastroenterology* **142**, 1160–1171 (2012).
- Sampath, V. et al. A functional ATG16L1 (T300A) variant is associated with necrotizing enterocolitis in premature infants. *Pediatr. Res.* **81**, 582–588 (2016).
- Burada, F. et al. ATG16L1 T300A polymorphism is correlated with gastric cancer susceptibility. *Pathol. Oncol. Res.* **22**, 317–322 (2016).
- Fujita, N. et al. Differential involvement of Atg16L1 in Crohn disease and canonical autophagy: analysis of the organization of the Atg16L1 complex in fibroblasts. *J. Biol. Chem.* **284**, 32602–32609 (2009).
- Wolfmeier, H. et al. Active release of pneumolysin prepores and pores by mammalian cells undergoing a *Streptococcus pneumoniae* attack. *Biochim. Biophys. Acta* **1860**, 2498–2509 (2016).
- Maekawa, M. & Fairn, G. D. Complementary probes reveal that phosphatidylserine is required for the proper transbilayer distribution of cholesterol. *J. Cell. Sci.* **128**, 1422–1433 (2015).
- Boucher, E. & Mandato, C. A. Plasma membrane and cytoskeleton dynamics during single-cell wound healing. *Biochim. Biophys. Acta* **1853**, 2649–2661 (2015).
- Jimenez, A. J. et al. ESCRT machinery is required for plasma membrane repair. *Science* **343**, 1247136 (2014).
- Andrews, N. W., Almeida, P. E. & Corrotte, M. Damage control: cellular mechanisms of plasma membrane repair. *Trends. Cell Biol.* **24**, 734–742 (2014).
- Corrotte, M., Castro-Gomes, T., Koushik, A. B. & Andrews, N. W. Approaches for plasma membrane wounding and assessment of lysosome-mediated repair responses. *Methods Cell Biol.* **126**, 139–158 (2015).
- Tinevez, J. Y. et al. Role of cortical tension in bleb growth. *Proc. Natl Acad. Sci. USA* **106**, 18581–18586 (2009).
- Anishkin, A. & Kung, C. Stiffened lipid platforms at molecular force foci. *Proc. Natl Acad. Sci. USA* **110**, 4886–4892 (2013).
- Xu, J. et al. Mechanism of polarized lysosome exocytosis in epithelial cells. *J. Cell. Sci.* **125**, 5937–5943 (2012).
- Ouimet, M. et al. Autophagy regulates cholesterol efflux from macrophage foam cells via lysosomal acid lipase. *Cell. Metab.* **13**, 655–667 (2011).
- Lu, F. et al. Identification of NPC1 as the target of U18666A, an inhibitor of lysosomal cholesterol export and Ebola infection. *eLife* **4**, e12177 (2015).
- Zanotti, I. et al. The LXR agonist T0901317 promotes the reverse cholesterol transport from macrophages by increasing plasma efflux potential. *J. Lipid Res.* **49**, 954–960 (2008).
- Lamason, R. L. & Welch, M. D. Actin-based motility and cell-to-cell spread of bacterial pathogens. *Curr. Opin. Microbiol.* **35**, 48–57 (2016).
- Grundling, A., Gonzalez, M. D. & Higgins, D. E. Requirement of the *Listeria monocytogenes* broad-range phospholipase PC-PLC during infection of human epithelial cells. *J. Bacteriol.* **185**, 6295–6307 (2003).
- Zhao, Z. et al. Autophagosome-independent essential function for the autophagy protein Atg5 in cellular immunity to intracellular pathogens. *Cell. Host. Microbe.* **4**, 458–469 (2008).
- Pavel, M. & Rubinsztein, D. C. Mammalian autophagy and the plasma membrane. *FEBS J.* **284**, 672–679 (2017).
- Murrow, L., Malhotra, R. & Debnath, J. ATG12-ATG3 interacts with Alix to promote basal autophagic flux and late endosome function. *Nat. Cell Biol.* **17**, 300–310 (2015).
- Maurer, K. et al. Autophagy mediates tolerance to *Staphylococcus aureus* alpha-toxin. *Cell Host Microbe.* **17**, 429–440 (2015).
- DeSelm, C. J. et al. Autophagy proteins regulate the secretory component of osteoclastic bone resorption. *Dev. Cell.* **21**, 966–974 (2011).
- Mrschtk, M. & Ryan, K. M. Lysosomal proteins in cell death and autophagy. *FEBS J.* **282**, 1858–1870 (2015).
- Huynh, K. K., Gershenson, E. & Grinstein, S. Cholesterol accumulation by macrophages impairs phagosome maturation. *J. Biol. Chem.* **283**, 35745–35755 (2008).
- Lebrand, C. et al. Late endosome motility depends on lipids via the small GTPase Rab7. *EMBO J.* **21**, 1289–1300 (2002).
- Ikonen, E. Cellular cholesterol trafficking and compartmentalization. *Nat. Rev. Mol. Cell Biol.* **9**, 125–138 (2008).
- Meyer-Morse, N. et al. Listeriolysin O is necessary and sufficient to induce autophagy during *Listeria monocytogenes* infection. *PLoS ONE* **5**, e8610 (2010).
- Bishop, D. K. & Hinrichs, D. J. Adoptive transfer of immunity to *Listeria monocytogenes*. The influence of in vitro stimulation on lymphocyte subset requirements. *J. Immunol.* **139**, 2005–2009 (1987).
- Jones, S. & Portnoy, D. A. Characterization of *Listeria monocytogenes* pathogenesis in a strain expressing perfringolysin O in place of listeriolysin O. *Infect. Immun.* **62**, 5608–5613 (1994).

53. Skoble, J., Portnoy, D. A. & Welch, M. D. Three regions within ActA promote Arp2/3 complex-mediated actin nucleation and *Listeria monocytogenes* motility. *J. Cell. Biol.* **150**, 527–538 (2000).
54. Shen, A. & Higgins, D. E. The 5' untranslated region-mediated enhancement of intracellular listeriolysin O production is required for *Listeria monocytogenes* pathogenicity. *Mol. Microbiol.* **57**, 1460–1473 (2005).
55. Gelber, S. E., Aguilar, J. L., Lewis, K. L. & Ratner, A. J. Functional and phylogenetic characterization of Vaginolysin, the human-specific cytolysin from *Gardnerella vaginalis*. *J. Bacteriol.* **190**, 3896–3903 (2008).
56. Wolfmeier, H. et al. Ca²⁺-dependent repair of pneumolysin pores: a new paradigm for host cellular defense against bacterial pore-forming toxins. *Biochim. Biophys. Acta* **1853**, 2045–2054 (2015).
57. Rescher, U., Zobiack, N. & Gerke, V. Intact Ca²⁺-binding sites are required for targeting of annexin 1 to endosomal membranes in living HeLa cells. *J. Cell. Sci.* **113**(Pt 22), 3931–3938 (2000).
58. Kabeya, Y. et al. LC3, a mammalian homologue of yeast Apg8p, is localized in autophagosome membranes after processing. *EMBO J.* **19**, 5720–5728 (2000).
59. Puri, C., Renna, M., Bento, C. F., Moreau, K. & Rubinsztein, D. C. Diverse autophagosome membrane sources coalesce in recycling endosomes. *Cell* **154**, 1285–1299 (2013).
60. Munsie, L. N., Caron, N., Desmond, C. R. & Truant, R. Lifeact cannot visualize some forms of stress-induced twisted F-actin. *Nat. Methods* **6**, 317 (2009).
61. Conway, K. L. et al. Atg16L1 is required for autophagy in intestinal epithelial cells and protection of mice from Salmonella infection. *Gastroenterology* **145**, 1347–1357 (2013).

Acknowledgements

We are grateful to E.A. Creasey, A. Draeger, V. Gerke, S. Grinstein, A. Hostettles, N. Mizushima, D. Portnoy, A. Ratner, D. Rubinsztein and R. Truant for providing reagents and advice, and to the SickKids Hospital Flow and Mass Cytometry Facility for help with flow cytometry. J.H.B. holds the Pitblado Chair in Cell Biology. Infrastructure

for the Brumell Laboratory was provided by a John Evans Leadership Fund grant from the Canadian Foundation for Innovation and the Ontario Innovation Trust. S.E.O. and N.M. were supported by a fellowship from the Research Training Centre at the Hospital for Sick Children. S.E.O. and J.H. were supported by CIHR fellowships. D.B. was supported by the Dutch Digestive Foundation. D.A.A. and M.A.C. were supported by a studentship from the Research Training Committee at the Hospital for Sick Children and an NSERC CGS-M scholarship. M.A.C. was supported by a University of Toronto Open Fellowship. M.C. was supported by an NSERC PGS-D scholarship and a CIHR Training Fellowship (no. TGF-53877). This work was supported by operating grants from The Arthritis Society of Canada (grant no. RG11/013) and the Canadian Institutes of Health Research (grant nos. MOP#97756, PJT#148668 and FDN154329).

Author contributions

J.H.B., J.M.J.T., N.M., S.E.O., J.H. and D.E.H. designed the experiments. J.M.J.T., N.M., S.E.O., D.A.A., D.D., R.L., D.B., J.M.v.R., M.A.C., M.C., E.C. and A.M.W. performed the experiments. C.M.Y., R.J.X., D.M., F.R., T.Y., J.D., G.D.F., B.R., P.K.K. and A.M.M. contributed reagents and consultations.

Competing interests

The authors declare no competing interests.

Additional information

Supplementary information is available for this paper at <https://doi.org/10.1038/s41564-018-0293-5>.

Reprints and permissions information is available at www.nature.com/reprints.

Correspondence and requests for materials should be addressed to J.H.B.

Publisher's note: Springer Nature remains neutral with regard to jurisdictional claims in published maps and institutional affiliations.

© The Author(s), under exclusive licence to Springer Nature Limited 2018

Life Sciences Reporting Summary

Nature Research wishes to improve the reproducibility of the work that we publish. This form is intended for publication with all accepted life science papers and provides structure for consistency and transparency in reporting. Every life science submission will use this form; some list items might not apply to an individual manuscript, but all fields must be completed for clarity.

For further information on the points included in this form, see [Reporting Life Sciences Research](#). For further information on Nature Research policies, including our [data availability policy](#), see [Authors & Referees](#) and the [Editorial Policy Checklist](#).

Please do not complete any field with "not applicable" or n/a. Refer to the help text for what text to use if an item is not relevant to your study. For final submission: please carefully check your responses for accuracy; you will not be able to make changes later.

▶ Experimental design

1. Sample size

Describe how sample size was determined.

Sample size was informed on the basis of: 1) limited availability of microscopy time for analysis and 2) the variability (within an experiment).

2. Data exclusions

Describe any data exclusions.

No data was excluded from analysis.

3. Replication

Describe the measures taken to verify the reproducibility of the experimental findings.

Findings were reproduced and observed in 3 cell lines in total, including knockout MEFs, knockout macrophages and knockdown HeLa cells.

4. Randomization

Describe how samples/organisms/participants were allocated into experimental groups.

Samples were allocated by genotype.

5. Blinding

Describe whether the investigators were blinded to group allocation during data collection and/or analysis.

Blinding was not possible since many cell types and cell genotypes were involved.

Note: all in vivo studies must report how sample size was determined and whether blinding and randomization were used.

6. Statistical parameters

For all figures and tables that use statistical methods, confirm that the following items are present in relevant figure legends (or in the Methods section if additional space is needed).

- | | |
|--------------------------|--|
| n/a | Confirmed |
| <input type="checkbox"/> | <input checked="" type="checkbox"/> The <u>exact sample size</u> (<i>n</i>) for each experimental group/condition, given as a discrete number and unit of measurement (animals, litters, cultures, etc.) |
| <input type="checkbox"/> | <input checked="" type="checkbox"/> A description of how samples were collected, noting whether measurements were taken from distinct samples or whether the same sample was measured repeatedly |
| <input type="checkbox"/> | <input checked="" type="checkbox"/> A statement indicating how many times each experiment was replicated |
| <input type="checkbox"/> | <input checked="" type="checkbox"/> The statistical test(s) used and whether they are one- or two-sided
<i>Only common tests should be described solely by name; describe more complex techniques in the Methods section.</i> |
| <input type="checkbox"/> | <input checked="" type="checkbox"/> A description of any assumptions or corrections, such as an adjustment for multiple comparisons |
| <input type="checkbox"/> | <input checked="" type="checkbox"/> Test values indicating whether an effect is present
<i>Provide confidence intervals or give results of significance tests (e.g. P values) as exact values whenever appropriate and with effect sizes noted.</i> |
| <input type="checkbox"/> | <input checked="" type="checkbox"/> A clear description of statistics including <u>central tendency</u> (e.g. median, mean) and <u>variation</u> (e.g. standard deviation, interquartile range) |
| <input type="checkbox"/> | <input checked="" type="checkbox"/> Clearly defined error bars in <u>all</u> relevant figure captions (with explicit mention of central tendency and variation) |

See the web collection on [statistics for biologists](#) for further resources and guidance.

► Software

Policy information about [availability of computer code](#)

7. Software

Describe the software used to analyze the data in this study.

Methods section contains this information.

For manuscripts utilizing custom algorithms or software that are central to the paper but not yet described in the published literature, software must be made available to editors and reviewers upon request. We strongly encourage code deposition in a community repository (e.g. GitHub). *Nature Methods* [guidance for providing algorithms and software for publication](#) provides further information on this topic.

► Materials and reagents

Policy information about [availability of materials](#)

8. Materials availability

Indicate whether there are restrictions on availability of unique materials or if these materials are only available for distribution by a third party.

Not applicable

9. Antibodies

Describe the antibodies used and how they were validated for use in the system under study (i.e. assay and species).

Methods section contains this information.

10. Eukaryotic cell lines

a. State the source of each eukaryotic cell line used.

Wild type and knockout MEFs and bone marrow derived macrophages were obtained from co-authors. HeLa CCL-2 cell stocks of low passage number (<5) were obtained from ATCC.

b. Describe the method of cell line authentication used.

Genotype of ATG knockouts confirmed by western blotting and RT-PCR. Additionally, western blotting for the autophagy protein LC3-B confirmed that its conjugation was defective in the ATG knockouts (a functional test). HeLa cells were confirmed morphologically and by western blotting.

c. Report whether the cell lines were tested for mycoplasma contamination.

All cell lines tested negative for mycoplasma prior to experimentation.

d. If any of the cell lines used are listed in the database of commonly misidentified cell lines maintained by [ICLAC](#), provide a scientific rationale for their use.

Not applicable.

► Animals and human research participants

Policy information about [studies involving animals](#); when reporting animal research, follow the [ARRIVE guidelines](#)

11. Description of research animals

Provide all relevant details on animals and/or animal-derived materials used in the study.

Mice bone marrow were obtained from co-authors.

Policy information about [studies involving human research participants](#)

12. Description of human research participants

Describe the covariate-relevant population characteristics of the human research participants.

Not applicable.